CM² MAGAZINE

第 40 期

南方科技大学海洋磁学中心主编

创刊词

海洋是生命的摇篮，是文明的纽带。地球上最早的生命诞生于海洋，海洋里的生命最终进化成了人类，人类的文化融合又通过海洋得以实现。人因海而兴。

人类对海洋的探索从未停止。从远古时代美丽的神话传说，到麦哲伦的全球航行，再到现代对大洋的科学钻探计划，海洋逐渐从人类敬畏崇拜幻想的精神寄托演变成可以开发利用与科学研究的客观存在。其中，上个世纪与太空探索同步发展的大洋科学钻探计划将人类对海洋的认知推向了崭新的纬度：深海（deep sea）与深时（deep time）。大洋钻探计划让人类知道，奔流不息的大海之下，埋藏的却是亿万年的地球历史。它们记录了地球板块的运动，从而使板块构造学说得到证实；它们记录了地球环境的演变，从而让古海洋学方兴未艾。

在探索海洋的悠久历史中，从大航海时代的导航，到大洋钻探计划中不可或缺的磁性地层学，磁学发挥了不可替代的作用。这不是偶然，因为从微观到宏观，磁性是最基本的物理属性之一，可以说，万物皆有磁性。基于课题组的学科背景和对海洋的理解，我们对海洋的探索以磁学为主要手段，海洋磁学中心因此而生。

海洋磁学中心，简称 CM^2，一为其全名“Centre for Marine Magnetism”的缩写，另者恰与爱因斯坦著名的质能方程 $E = MC^2$ 对称，借以表达我们对科学巨匠的敬仰和对科学的不懈追求。

然而科学从来不是单打独斗的产物。我们以磁学为研究海洋的主攻利器，但绝不仅限于磁学。凡与磁学相关的领域均是我们关注的重点。为了跟踪反映国内外地球科学特别是与磁学有关的地球科学领域的最新研究进展，海洋磁学中心特地主办 CM^2 Magazine，以期与各位地球科学工作者相互交流学习、合作共进！

“海洋孕育了生命，联通了世界，促进了发展”。 21 世纪是海洋科学的时代，由陆向海，让我们携手迈进中国海洋科学的黄金时代

目 录

CM2 研究进展

QSR：亚北极太平洋风尘和火山灰 Fe 施肥效应对比

南大洋、亚北极太平洋和赤道东太平洋是典型的高营养盐低叶绿素（HNLC）区域。在这些地区以硅藻为主导的初级生产力主要受微量元素铁的限制。大陆风尘通过大气环流可为开阔大洋提供丰富的铁。因此，John Martin 在上世纪 80 年代提出了有名的“铁假说”：在冰期期间，大陆风尘来源 Fe 向大洋输入增多，促进硅藻等初级生产力的生长，增加有机碳的埋藏，进而降低全球大气 CO_2 含量，并使全球气候变冷（图 1）。

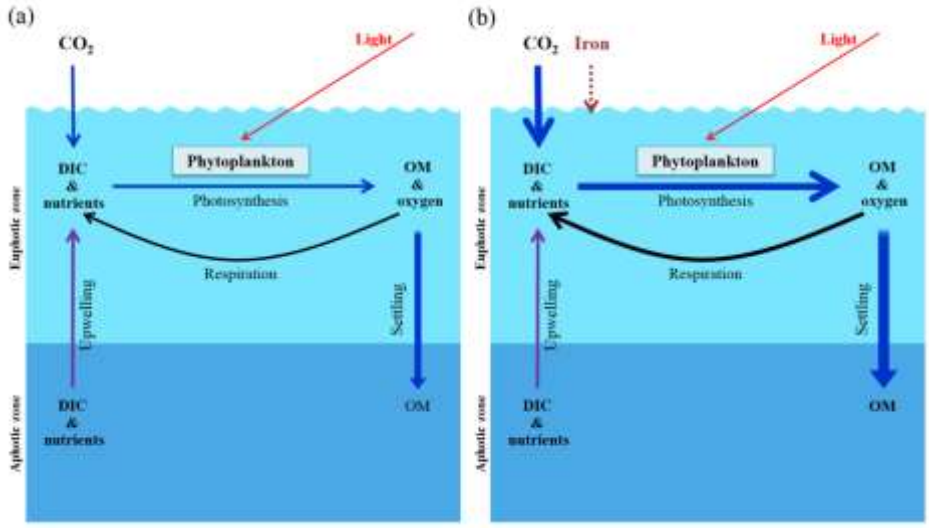

图 1. Fe 假说：Fe 输入对生产力和有机碳埋藏的促进作用，after Yoon et al., 2018

自“铁假说”提出以来，在南大洋、亚北极太平洋和赤道东太平洋开展的现代 Fe 投实验大部分表明 Fe 施肥可以促进这些地区硅藻等初级生产力的生长。然而，Fe 假说在地质历史时期是否成立还存在较多争议。其原因，一方面在于自然条件下 HNLC 大洋区域有多种 Fe 来源。除了风尘输入能够带来大量铁以外，火山灰、冰筏碎屑、河流、大陆沿岸沉积物释放等都可为大洋输入铁元素。另一方面，

陆源输入铁的溶解度和生物利用效率受到含铁矿物的含量、类型、颗粒大小等性质的影响。因此，为深入理解地质历史时期风尘 Fe 施肥效应需要详细的区分 Fe 输入来源以及含铁矿物类型、颗粒大小等性质。

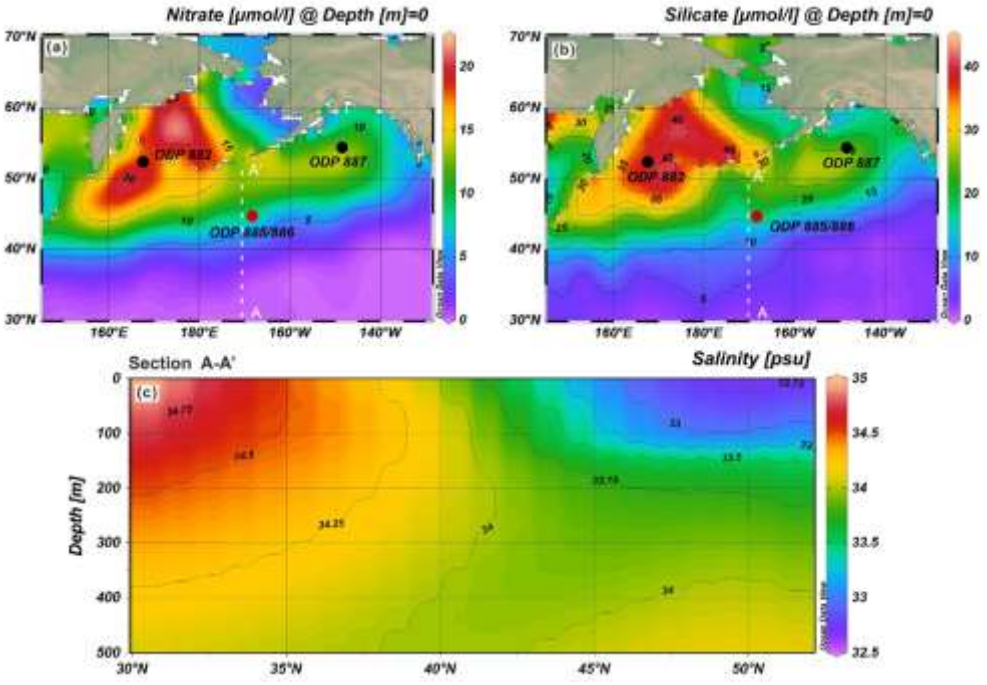

图 2 研究区域与 ODP 885 孔位置

针对以上问题，南方科技大学海洋科学与工程系海洋磁学中心刘青松团队联合澳大利亚国立大学地球科学学院 Andrew Roberts 教授、中国海洋局第一海洋研究所石学法教授等，选取亚北极太平洋南部 ODP （大洋钻探计划）885 站位 2.8–0.9 Ma 沉积物为研究载体（图 2）。该站位远离大陆边缘，不受冰筏碎屑、河流以及沿岸沉积物 Fe 输入的影响，其沉积物主要由来源亚洲内陆的风尘和内源硅藻组成，在部分层段含有火山灰。因此，该站位是检验亚洲风尘和火山灰对硅藻铁施肥效应的理想场所。通过对该站位 2.8-0.9 Ma 沉积物中硅藻属种鉴定以及含量变化的研究，并与该孔详细的岩石磁学结果和全球气候变化研究结果做对比，发现亚洲风尘对硅藻生长的铁施肥效应不明显，而火山灰输入对硅藻的铁施肥效应相对更显著。主要原因在于亚洲风尘中含铁矿物主要由包裹在硅酸盐矿物内的单畴（钛）磁铁矿、颗粒较大的多畴磁铁矿以及针铁矿和赤铁矿组成，这些含铁磁性矿物都不易被溶解和被硅藻利用，因此，对硅藻生长的促进作用不明显。而火山灰层段磁性矿物含量显著升高，而且以纳米级为主的细颗粒 SP/SD 磁性矿

物含量较高，这些细颗粒 SP/SD 含铁磁性颗粒在海水中相对更容易溶解，利于被硅藻利用。

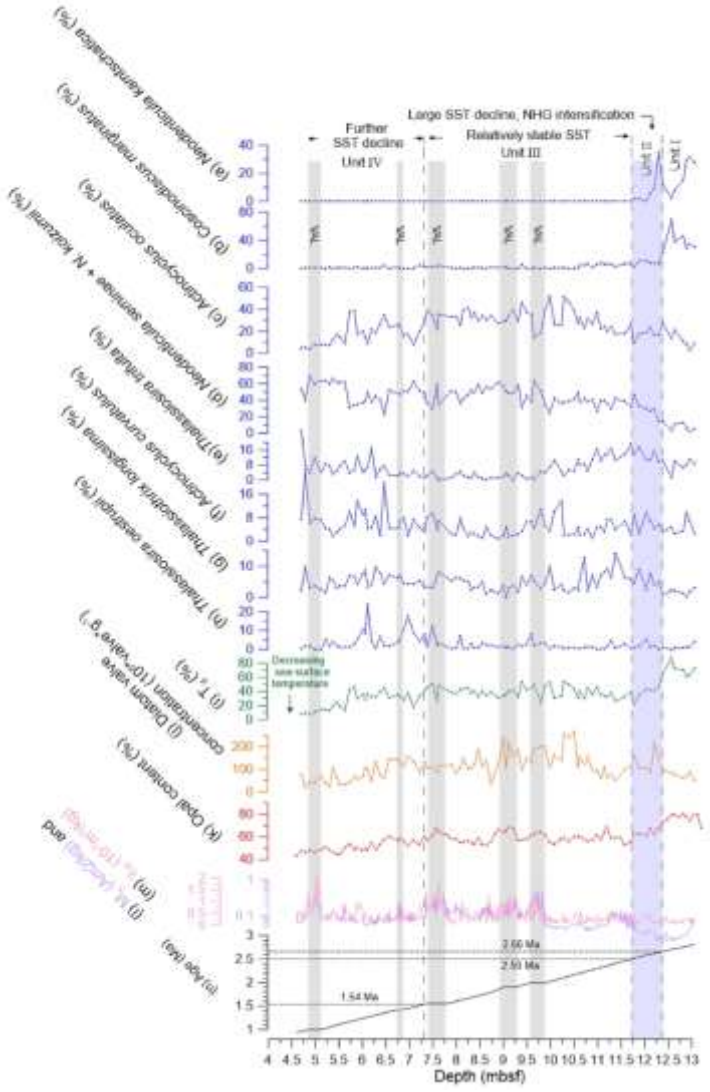

图3. ODP 885站位2.8–0.9 Ma期间硅藻种群变化与磁学参数χ_{fd}和M_s（Zhang et al., 2018）对比，图中灰色阴影部分（VAL）指示含火山灰层段

该研究还表明，在 2.66 Ma 之前，即北半球冰川作用加强（iNHG）之前，因上升流作用强盛，主量营养盐输入丰富，硅藻生产力最高。2.66–1.54 Ma 期间硅藻属种变化和生产力降低与该阶段亚北极太平洋海表温度降低和水体分层加强相对应。1.54–0.9 Ma 期间硅藻属种和生产力变化与 1.5 Ma 之后全球气候进一步变冷对应，并可能指示了亚北极太平洋的进一步分层。

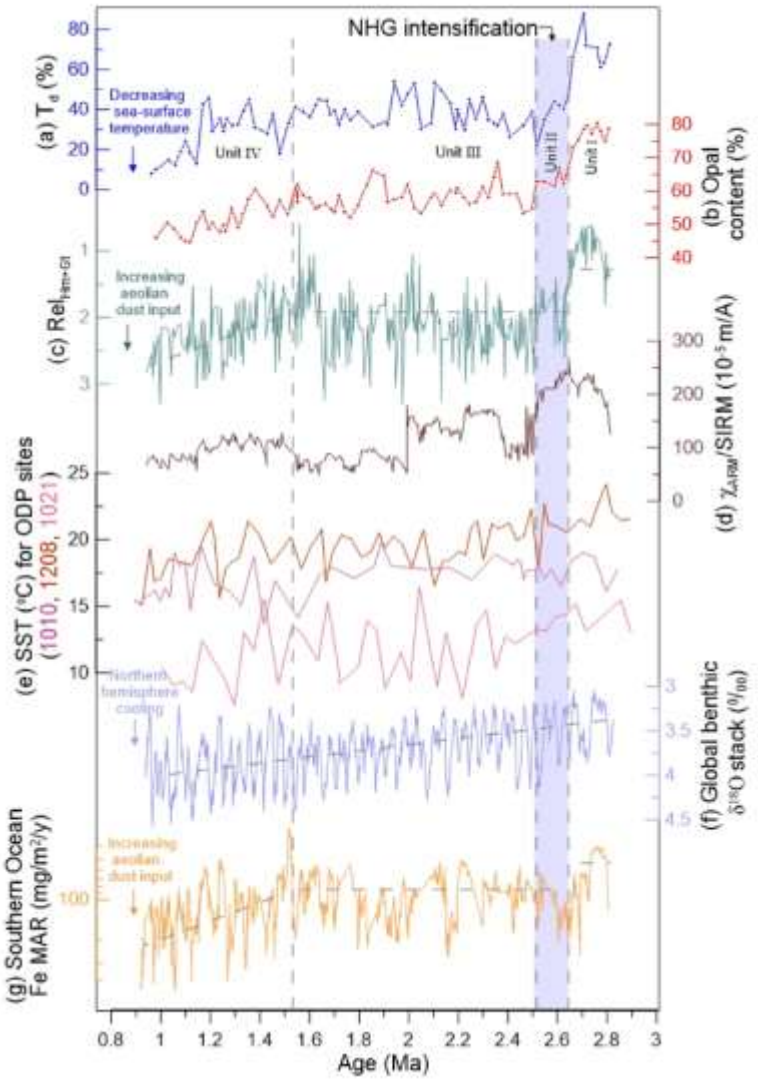

图 4. ODP 885 站位 2.8–0.9 Ma 硅藻记录反映的海表温度变化（a）和蛋白石含量（b）与亚洲风尘输入（c）以及全球其他气候记录综合对比

文章来源：Chen, T., Q. S. Liu, A. Roberts, X. F. Shi, and Q. Zhang (2020), A test of the relative importance of iron fertilization from aeolian dust and volcanic ash in the stratified high-nitrate low-chlorophyll subarctic Pacific Ocean, Quaternary Science Reviews, 106577.

论文第一作者为陈艇博士，研究领域包括古地磁学与环境磁学、沉积硅藻学、古海洋学等；近期研究主要集中在西北太平洋亚洲风尘输入的生物环境效应和中国边缘海近百年磁性地层与环境污染。

参考文献：

Yoon, J.E., Yoo, K.C., Macdonald, A.M., Yoon, H.I., Park, K.T., Yang, E.J., Kim, H.C., Lee, J.I., Lee, M.K., Jung, J., Park, J., Lee, J., Kim, S., Kim, S.S., Kim, K., Kim, I., 2018. Reviews and syntheses: Ocean iron fertilization experiments - past, present, and future looking to a future Korean Iron Fertilization Experiment in the Southern Ocean (KIFES) project. Biogeosciences 15, 5847-5889.

Zhang, Q., Liu, Q., Li, J., Sun, Y., 2018. An integrated study of the eolian dust in pelagic sediments from the North Pacific Ocean based on environmental magnetism, transmission electron microscopy, and diffuse reflectance spectroscopy. Journal of Geophysical Research: Solid Earth 123, 3358-3376.

第 30 章　磁黄铁矿

大学实习时，去武汉大冶铁矿，拿着地质锤在岩石上敲下来一块金灿灿的黄铁矿（Pyrite，FeS_2）。这是我第一次亲自得到铁硫化物的标本，内心非常喜悦。当接触到岩石磁学这门学科后，才得知居然还有带磁性的黄铁矿。

黄铁矿是一个门类，自然界中有磁黄铁矿 $Fe_{1-x}S$（$0<x<0.13$）（Pyrrhotite）。我们考虑两种磁黄铁矿：单斜（Monoclinic）晶系（Fe_7S_8，$x = 0.125$），以及六方晶系（Hexagonal Fe_9S_{10}，$x = 0.1$；$Fe_{11}S_{12}$，$x = 0.083$)。

单斜晶系磁黄铁矿 Fe_7S_8 具有亚铁磁性，其晶胞参数：

$a = 1.190$ nm

$b = 0.687$ nm

$c = 2.281$ nm

$T_C = \sim 320℃$

$M_S = 15\ Am^2/kg = 1/6$ 磁铁矿 M_S

单斜磁黄铁矿具有较高的磁结晶各向异性，SD 磁黄铁矿的矫顽力要比 SD 磁铁矿的高，其 SD 上边界是 1.6 μm。

$0.2 < M_{rs} / M_s < 0.6$

单斜磁黄铁矿的 FORC 图也是牛眼状，但是其中心矫顽力会更高些。

单斜磁黄铁矿的磁性来源在于其晶格内存在不少的铁空位，因而形成亚铁磁性。

通过分析磁铁矿、胶黄铁矿和单斜磁黄铁矿，我们可以清晰地得出，其磁结晶各向异性能和 M_s 成反比。M_s 越小，磁结晶各向异性能越大，矫顽力越高，SD 的上边界也就越大。

单斜磁黄铁矿一般为 SD 颗粒，可以稳定地记录剩磁信息，它在自然界中分布也很广，尤其在花岗岩（Jover et al.，1989）、岩浆岩（Rochette et al.， 1987）、

玄武岩岩墙（Soffel et al., 1981）、以及蛇绿岩（Lorand et al.，1987）、变质岩（Appel et al., 2012）等岩石都发现过其踪迹。

这说明单斜磁黄铁矿的生成与高温高压有关系。在硫化物处于热稳定状态的岩石中，单斜磁黄铁矿可以提供十分重要的古地磁信息。

单斜磁黄铁矿在低温也有一个特征转换点（Besnus 转换），在 30-34 K，其剩磁会发生剧烈变化，这是用低温技术检测单斜磁黄铁矿的重要特征。

早期研究磁黄铁矿比较多的是 Pierre Rochette 教授、Mark Dekkers 教授。后期 Andrew Roberts 教授、洪崇胜教授等对台湾地区的磁黄铁矿进行了细致研究。从台湾来的碎屑物中含有铁硫化物，因此，在冲绳海槽，铁硫化物一般认为来源于台湾。

在青藏高原地区，由于印度碰撞产生区域变质作用，磁黄铁矿在青藏高原南缘的岩石中广泛存在，造成重磁化现象。在这方面 Erwin Appel 教授做了很好的综述（Appel et al., 2012）。

第二种磁黄铁矿是六方晶系磁黄铁矿，它的晶型是对称的，所以不存在铁空位，因此，它具有反铁磁性。但是，在 200 ℃ 时，六方晶系磁黄铁矿由反铁磁性转化为亚铁磁性，主要是热扰动促使晶格空位定向排列引起。这个特征是检测这种六方晶系磁黄铁矿的主要证据之一。

“偶遇”丁文江先生

陈 艇

第一次见到丁文江这个名字，是写博士毕业论文期间，要查找论述是否在全新世以前长江有分流古河道经过芜湖—高淳—溧阳—宜兴—湖州——杭州一线进入杭州湾的文献。这是长江三角洲古环境研究中极不引人注意的小问题。资料很少，查到少数几篇可以引用的文献里面有一篇是丁文江先生1917年的文章，文中说丁文江先生有考察过高淳-溧阳-宜兴一带。当时，有眼不识泰山，只是心里犯嘀咕原来那么早还有人关注这个“小问题”。最近看贾兰坡先生的《爷爷的爷爷从哪里来》说到在周口店北京人的发掘过程中，丁文江先生大力支持，并极力促进新生代环境实验室的成立。也？被抓住了眼球。然后查阅了关于丁文江先生的文献。有很多研究科技史的论文论述丁文江先生的成就，也有胡适先生为他写的传记《丁文江先生》。这么一个泰斗极的人物无需我再做介绍。只是想说说看了关于丁先生生平伟绩之后自己的一点感触。

丁文江先生在格拉斯哥大学学习了地质学和动物学（难怪他对北京人的发掘这么关注，这正好是两个学科交叉的契合点），回国主持地质学方面的研究，但是当时国内地质学人才几乎为零，丁先生负责组织培训地质学人才。丁先生在教学生时极其注重学生的实地观察、动手、实践能力。这点我深以为意。可能有人会说现在全国各大与地学有关的院校每年都会组织学生参加野外实践，这有什么稀奇？

我在前两年暑假有幸跟着南科大的学生们去了柳江盆地实习。正直暑假实习高峰期，队伍一波接一波。在有个点上，我们的学生做好了岩性描述、产状测量、示意图的绘制等。后面跟着另外一个学校的学生，大概有五六十号人，而我们只有二十人左右，在他们没有开始之前，就在想这么多人，怎么完成这个点的观测、测量和作图？想一探究竟。首先是他们的老师站在这个点上，讲了与这个点相关的地质现象、原因以及地质意义，对面是学生在听和做笔记。这个老师讲的很仔细也很系统，学生先了解下背景，自己再做观察应该也少了很多盲目。等他讲完了，想看看他们是怎么分组做考察的。可是，等老师讲完了，所有的学生又跟着去了下一个点……。所以，现在有的高校的野外地质实习，真的是野外地质实习么？还

是只是封闭式的课堂挪了一个位置？

还有一点，说来可能有点好笑。在正好读到“在三几年动乱年代丁文江先生组织几个队伍到四川、云南、贵州做详细的地质考察，其中一个队友在贵州考察时遇到土匪，被打死了”时，一个正在读博士的师弟说文章被拒了，感觉要绝望了，当即就发了这段描述给他。实验重做、论文被拒、延期毕业等等很多学生都会遇到，而在生死面前这些都是小事，坚持下去就是胜利。

丁先生 49 岁时在湖南**煤矿做调查期间，因生病在家中调养，不幸因煤气中毒而亡故。非常可惜的是，丁先生本人做了很多地质实地考察，但是这些考察材料都没有来得及整理成文。这一点是用来反思自己的：脑子里时常有很多想法，一段时间过后，发现想法还是想法，总是疏于行动。所以，今早想到这儿，一咕噜爬起来，先完成这篇小文再说。

文献速递

1. 一个天文调谐年代的地球气候记录及其过去 66 百万年以来的可预测性

翻译人：仲义 zhongy@sustech.edu.cn

Thomas Westerhod, Norbert Marwan, Anna Joy Drury et al.,* ***An astronomically dated record of Earth's climate and its predictability over the last 66 million years*** *[J] Science, 2020, 369, 1381-1387.*

https://science.sciencemag.org/content/369/6509/1383/tab-pdf

摘要：通过深海底栖有孔虫的碳、氧同位素结果可以认识地球演化的历史。然而，现有的长时间周期记录中缺少对新生代以来气候模态类型和动态研究所需要的时间分辨率和年龄控制。因此，作者基于高精度天文调谐定年法获得完整的底栖有孔虫同位素记录。通过温室气体含量和极地冰盖体积对天文轨道响应的不同反应程度划分为四个气候模态–高温室、暖室、低温室及冰室阶段。进而，通过统计学分析显示非线性行为特征存在该记录中，说明极地冰盖体积对新生代气候预测性发挥重要的作用。

ABSTRACT: Much of our understanding of Earth's past climate comes from the measurement of oxygen and carbon isotope variations in deep-sea benthic foraminifera. Yet, long intervals in existing records lack the temporal resolution and age control needed to thoroughly categorize climate states of the Cenozoic era and to study their dynamics. Here, we present a new, highly resolved, astronomically dated, continuous composite of benthic foraminifer isotope records developed in our laboratories. Four climate states—Hothouse, Warmhouse, Coolhouse, Icehouse—are identified on the basis of their distinctive response to astronomical forcing depending on greenhouse gas concentrations and polar ice sheet volume. Statistical analysis of the nonlinear behavior encoded in our record reveals the key role that polar ice volume plays in the predictability of Cenozoic climate dynamics.

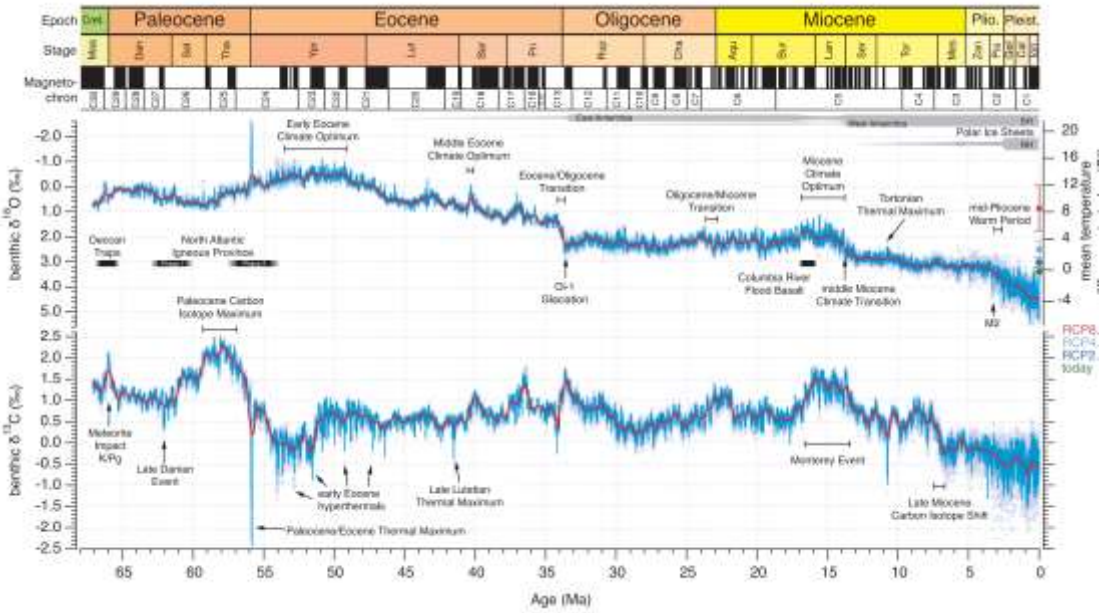

Figure 1. Cenozoic Global Reference benthic foraminifer carbon and oxygen Isotope Dataset (CENOGRID) from ocean drilling core sites spanning the past 66 million years. Data are mostly generated by using benthic foraminifera tests of the taxa Cibicidoides and Nuttallides extracted from carbonate-rich deepsea sediments drilled during Ocean Drilling Program (ODP) and Integrated Ocean Drilling Program (IODP) expeditions. Genus-specific corrections were applied and oxygen isotope data adjusted by +0.64‰ and +0.4‰, respectively (12), with the green dot indicating the average oxygen isotope composition of the last 10 kyr. Average resolution for the interval from 0 to 34 Ma is one sample every 2 ky; for the interval from 34 to 67 Ma, it is one sample every 4.4 kyr. After binning, data were resampled and smoothed by a locally weighted function over 20 kyr (blue curve) and 1 Myr (red curve) to accentuate the different rhythms and trends in Earth's carbon cycle and temperature operating on various time scales. Oxygen isotope data have been converted to average temperature differences with respect to today (13). Future projections for global temperature (44) in the year 2300 are shown by plotting three representative concentration pathways (RCP) scenarios (light blue, dark blue, and red dots). Gray horizontal bars mark rough estimates of ice volume in each hemisphere. Absolute ages for epochs and stages of the Cenozoic (GTS2012) and geomagnetic field reversals (this study) are provided for reference. The oxygen isotope data axis is reversed to reflect warmer temperatures at times of lower d18O values. Aqu, Aquitanian; Bur, Burdigalian; Cal, Calabrian; Cha, Chattian; Cret.,

Cretaceous; Dan, Danian; Gel, Gelasian; Ion, Ionian; K/Pg, Cretaceous/Paleogene boundary; Lan, Langhian; Lut, Lutetian; M2, first major glacial event in the NH; Maa, Maastrichtian; Mes, Messinian; NH, Northern Hemisphere; Oi-1, the first major glacial period in the Oligocene; Pia, Piacenzian; Pleist., Pleistocene; Plio., Pliocene; Pri, Priabonian; Rup, Rupelian; Sel, Selandian; Ser, Serravallian; SH, Southern Hemisphere; Tha, Thanetian; Tor, Tortonian; Ypr, Ypresian; Zan, Zanclean.

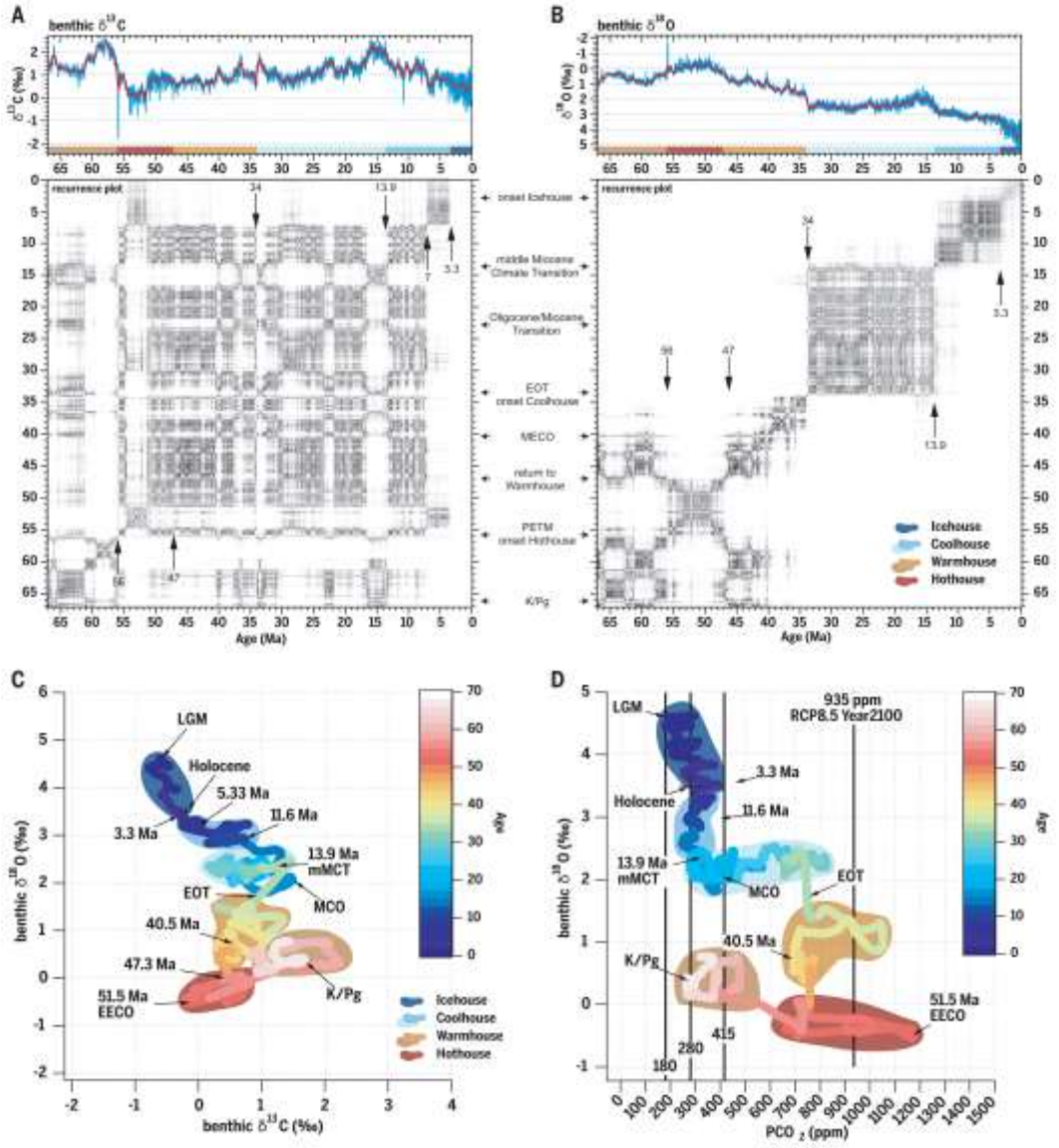

Figure 2. Climate states of the Cenozoic. Deep-sea benthic foraminifer high-resolution carbon (A) and oxygen (B) isotope records and the respective recurrence plots as well as scatterplots of long-term benthic foraminifer carbon versus oxygen values (C) and oxygen values versus atmospheric CO2 concentrations (D). Recurrence analysis compares climate change patterns occurring in a specific interval to the entire record. If climate dynamics have similar patterns, they will show up as darker

areas in the plot; if they have no common dynamics, the plot will remain white. Four distinct climate states can be identified as Hothouse, Warmhouse, Coolhouse, and Icehouse with distinct transitions among them. The relation of oxygen isotopes, representative for average global temperature trends, to atmospheric CO2 concentrations suggests that the present climate system as of today [415 parts per million (ppm) CO2] is comparable to the Miocene Coolhouse close to the MCO. If CO2 emissions continue unmitigated until 2100, as assumed for the RCP8.5 scenario, Earth's climate system will be moved abruptly from the Icehouse into the Warmhouse or even Hothouse climate state. LGM, Last Glacial Maximum; MECO, Middle Eocene Climate Optimum; PETM, Paleocene/Eocene Thermal Maximum.

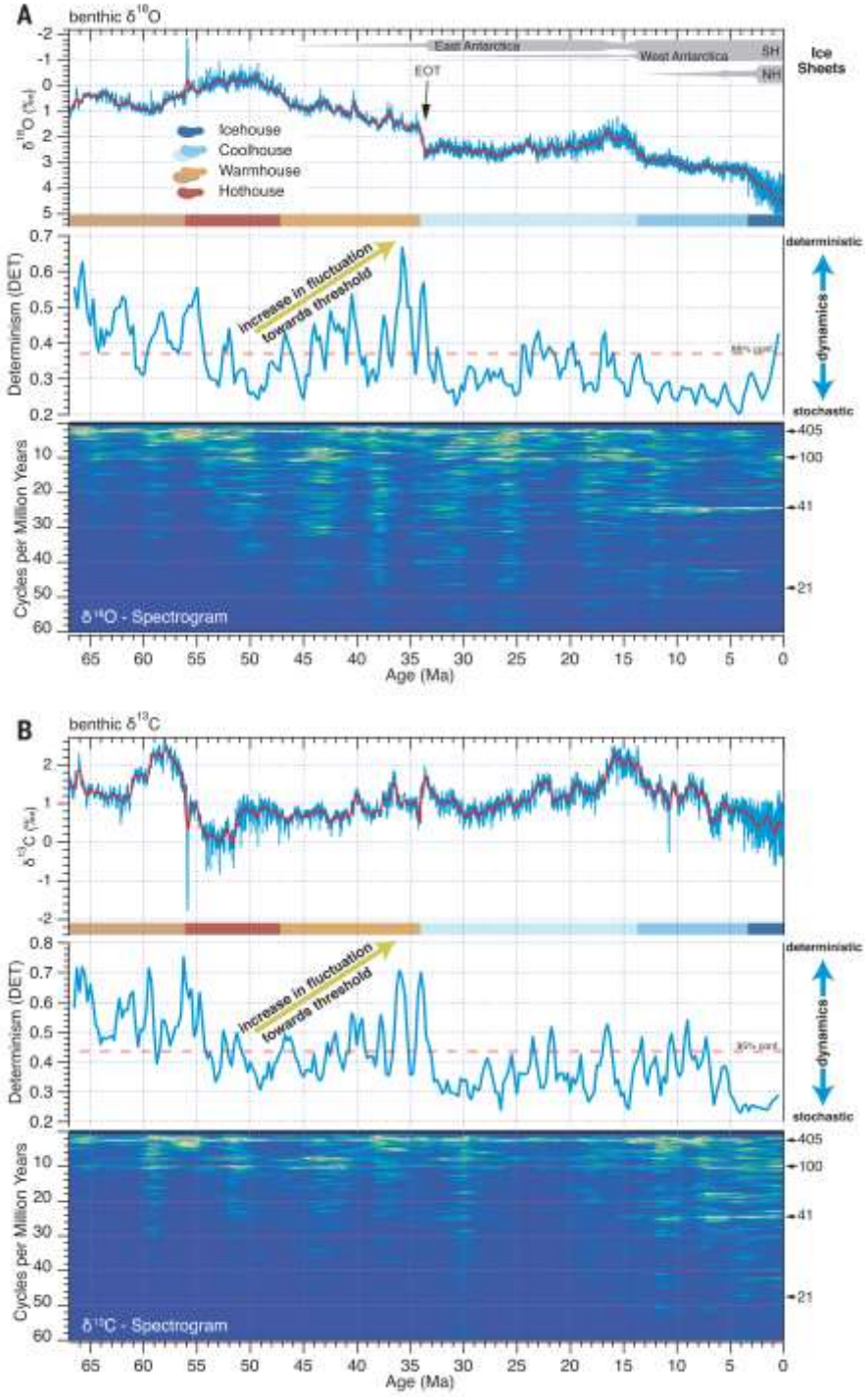

Figure 3. Quasi-periodic changes and determinism in the global reference carbon cycle and oxygen isotope record. Evolutionary fast Fourier transform (FFT) spectrogram, recurrence determinism analysis, and benthic foraminifer oxygen (A) and carbon (B) isotope data plotted on age with the four climate states. Frequencies between 2 and 60 cycles per million years are related to changes in Earth's orbital parameters, known as Milankovitch cycles. The FFT spectrograms were computed with a 5-Myr

window on the detrended records of benthic carbon and oxygen isotope data. From 67 to 13.9 Ma, cyclic variations in global climate are dominated by the eccentricity cycles of 405 and 100 kyr. Thereafter, in particular in the oxygen isotope record, the influence of obliquity increased, dominating the rhythm of climate in the record younger than ~7.7 Ma. Recurrence analysis of determinism (DET) shows that climate in the Warmhouse state is more deterministic (predictable) than in the Hothouse, Coolhouse, and Icehouse. From 47 Ma toward the EOT at 34 Ma, climate dynamic changes are rising in amplitude, approaching a threshold in the climate system. If DET tends to low values, the dynamics are stochastic, whereas high values represent deterministic dynamics.

2. 二叠纪末生物大灭绝期间营养控制的海洋缺氧

翻译人：蒋晓东 jiangxd@sustech.edu.cn

Schobbeb M, Foster W. J, Sleveland A R N, et al. ***A nutrient control on marine anoxia during the end-Permian mass extinction*** *[J]. Nature Geoscience, 2020, 13, 640-646.*

https://doi.org/10.1038/s41561-020-0622-1

摘要：在二叠纪–三叠纪（~259.1 Ma）间，缺氧和硫化物毒害作用是被认为是引起生物大灭绝的主要因素。然而这两个因素驱动海洋中形成大范围缺氧的机制仍然是不清楚的。本研究在斯瓦尔巴特群岛执行了海洋横切面测深，并获得古氧化还原和多种类磷等数据。结果表明在大灭绝前增强的西伯利亚暗色岩风化增加了磷的流通量，因此增强了陆架近端海洋初级生产力和缺氧状态。然而，这种非硫磺酸状态有效扣押了沉积物中与铁矿物相关的磷，因而限定了缺氧海水的强度和空间幅度。在海洋大灭绝前陆地植被的崩塌改变了来自风化作用的铁和硫的流通量，产生的静水（硫化的）条件引起生物可利用磷重新活化的增强。该作用引起缺氧海水在陆架区域大尺度扩张。这一机制可以解释风化作用开始到广泛发展间约 0.3 Ma 滞后，但是地理上的可变性、海洋缺氧，很大程度上意味着大灭绝的选择性。

ABSTRACT: Oxygen deprivation and hydrogen sulfide toxicity are considered potent kill mechanisms during the mass extinction just before the Permian–Triassic boundary (~251.9 million years ago). However, the mechanism that drove vast stretches of the ocean to an anoxic state is unclear. Here, we present palaeoredox and phosphorus speciation data for a marine bathymetric transect from Svalbard. This shows that, before the extinction, enhanced weathering driven by Siberian Traps volcanism increased the influx of phosphorus, thus enhancing marine primary productivity and oxygen depletion in proximal shelf settings. However, this non-sulfidic state efficiently sequestered phosphorus in the sediment in association with iron minerals, thus restricting the intensity and spatial extent of oxygen-depleted waters. The collapse of vegetation

on land immediately before the marine extinction changed the relative weathering influx of iron and sulfate. The resulting transition to euxinic (sulfidic) conditions led to enhanced remobilization of bioavailable phosphorus, initiating a feedback that caused the spread of anoxic waters across large portions of the shelf. This reconciles a lag of >0.3 million years between the onset of enhanced weathering and the development of widespread, but geographically variable, ocean anoxia, with major implications for extinction selectivity.

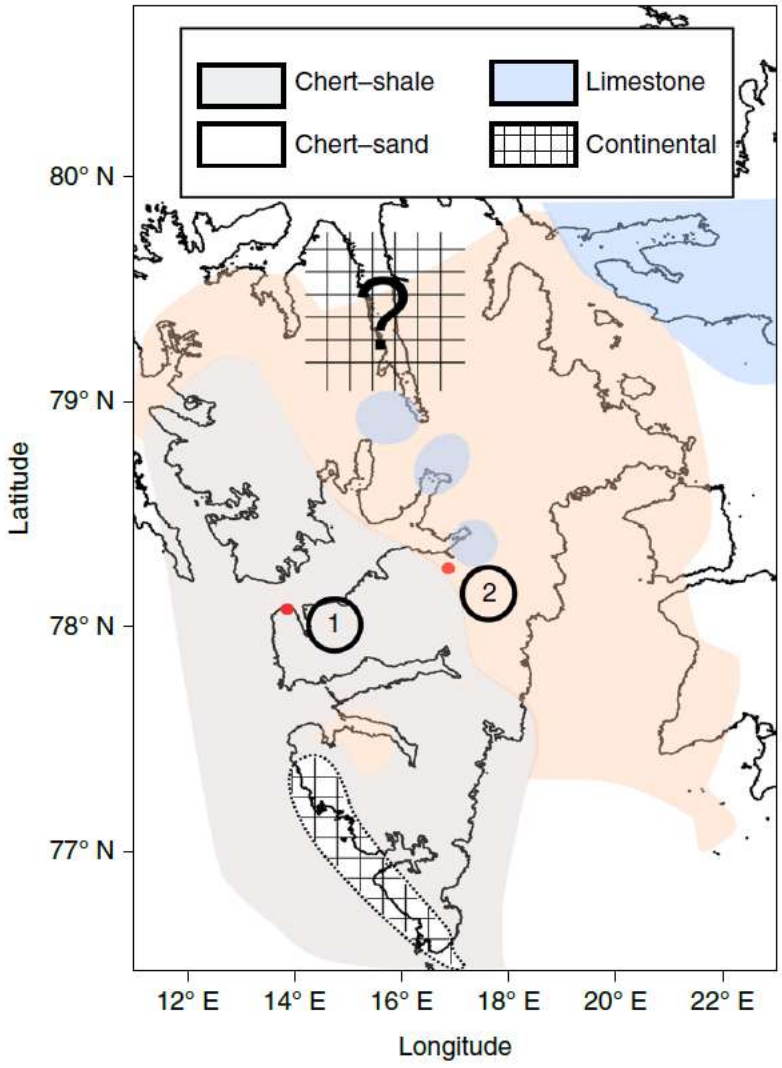

Figure 1. Geographical setting of the Festningen section and Deltadalen core. Late Permian lithofacies of Svalbard after ref. 29 and section 2 of the Supplementary Information. The tentative location of a northern source area (possibly on the Nordfjorden High) is demarcated with a question mark; the S 鴕 kapp-Hornsund High is encircled with a dotted line. The red dots mark the exact locations of the Festningen section (1) and Deltadalen core (2). Base map from GADM database (https://gadm.org/).

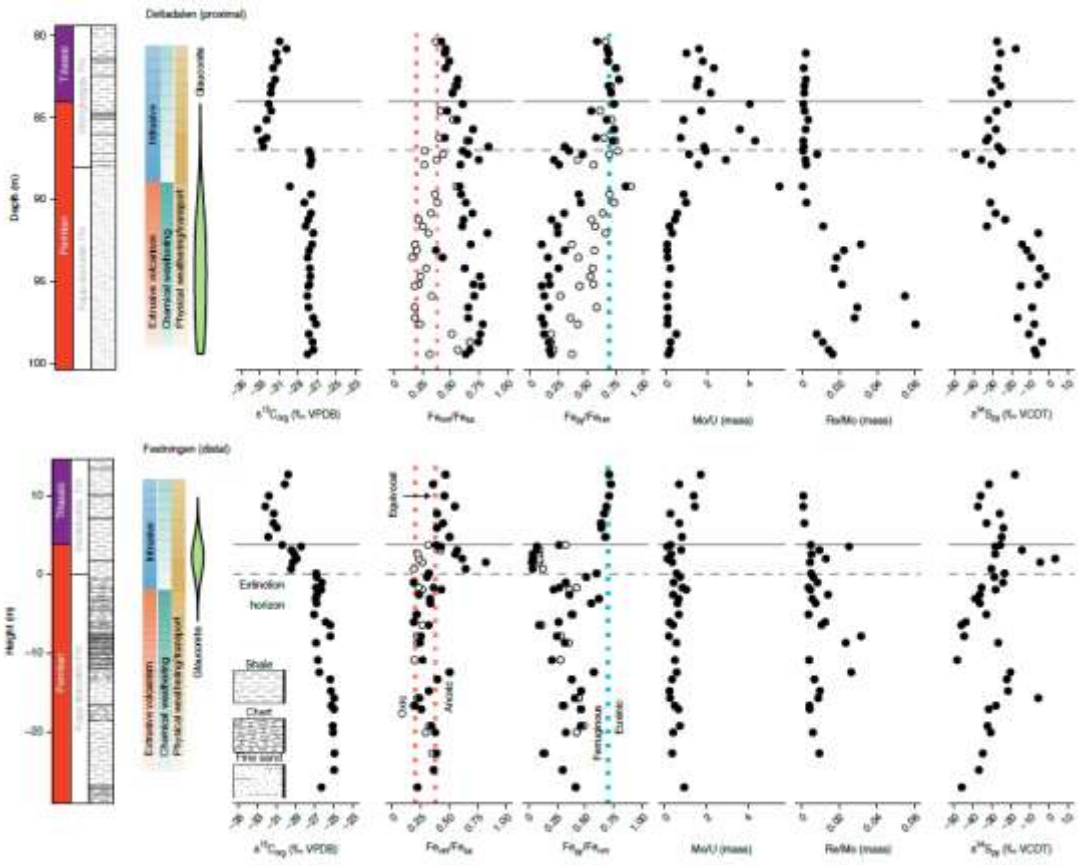

Figure 2. Stratigraphic plot of $\delta^{13}C_{org}$, Fe speciation, Mo/U, Re/Mo and $\delta^{34}S_{py}$ for the Festningen outcrop and Deltadalen core. The boundaries (vertical dotted lines) for oxic, anoxic, ferruginous (Fe(II)-rich) and euxinic (H2S-$_{rich}$) water-column conditions were calibrated in modern and ancient aquatic environments (see text for sources). Iron speciation (Fe_{py}/Fe_{HR}*, Fe_{HR}/Fe_{tot}*) corrected for excess Fe_{PRS} (excess Fe_{PRS} = (measured Fe_{PRS}/Fe_{tot} − baseline Fe_{PRS}/Fe_{tot}) × Fe_{tot} if measured Fe_{PRS}/Fe_{tot} > baseline Fe_{PRS}/Fe_{tot}) is shown as black circles; uncorrected values are shown as open circles (see section 7.2 of the Supplementary Information). Subscripts of isotope ratios: org, organic carbon; py, pyrite. Fe_{HR} = Fe_{carb} (iron bound to carbonate) + Fe_{ox} (iron bound to Fe oxy(hydr)oxides) + Fe_{mag} (iron bound as magnetite) + Fe_{py}. Reproducibility for Fe_{py} and Fe_{HR} is better than 5% and 9% relative standard deviations (RSDs), better than 8% RSD for total elemental concentrations, and better than 0.1‰ and 0.9‰ s.d. for $\delta^{13}C_{org}$ and $\delta^{34}S_{py}$. Horizontal dashed grey line, extinction event; solid grey line, P – Tr boundary. Details on lithology and stratigraphy in Supplementary Fig. 2 and sections 2 and 3 of the Supplementary Information.VPDB, Vienna PeeDee Belemnite; VCDT, Vienna Canyon Diablo Troilite.

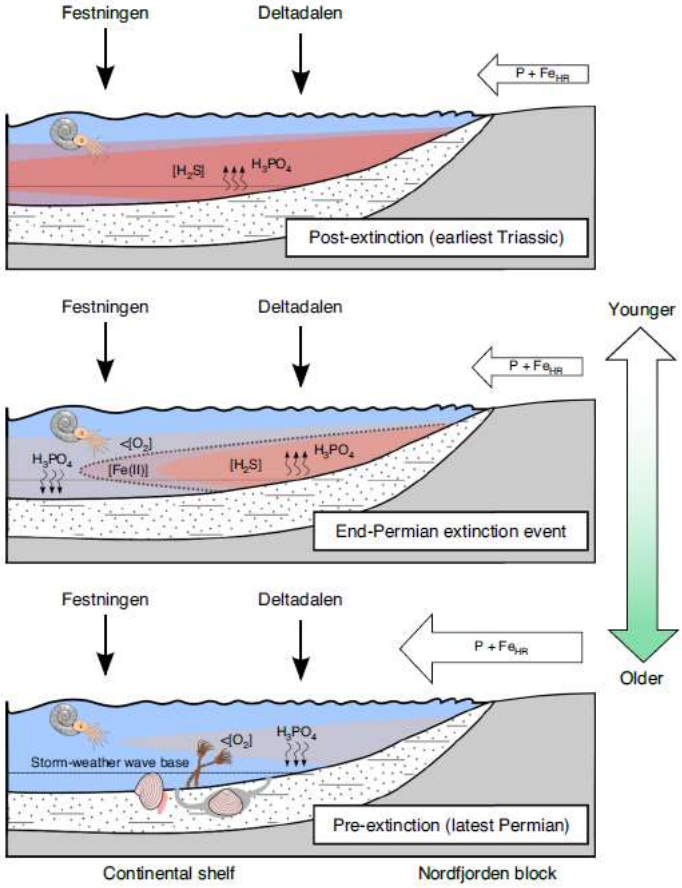

Figure 3. Conceptual model of the development of water-column redox conditions. In the latest Permian, the inner shelf was dysoxic (demarcated with $<[O_2]$), and large amounts of reactive P accumulated, whereas the outer shelf harboured a thriving ecosystem (here depicted as crinoids and molluscs, but which are not representative of the actual fossil assemblages). During the end-Permian mass extinction, euxinia (demarcated with $[H_2S]$) developed on the inner shelf, whereas the outer shelf environment became dysoxic/ferruginous (demarcated with [Fe(II)]). Under these conditions, P was remobilized as dissolved P (demarcated with H_3PO_4) from the inner shelf, invigorating productivity (and thus oxygen depletion), and dissolved P was recycled to the outer shelf and initially deposited through uptake by Fe (oxyhydr)oxide particles settling on the seabed. After the extinction, euxinic conditions became more prevalent across the shelf, initiated and maintained by recycling of P.

3. 青藏高原中部增厚的下地壳发生拆沉后，其地表隆升可忽略不计

翻译人：冯婉仪 fengwy@sustech.edu.cn

Zeng Y C, Ducea M N, Xu J F, et al. Negligible surface uplift following foundering of thickened central Tibetan lower crust[J]. Geology, 2020, 48.

https://doi.org/10.1130/G48142.1

摘要：本研究利用羌塘地块始新世埃达克岩（EARs）的单斜辉石（cpx）组成和锆石 Hf-O 同位素来解析青藏高原中部的形成机制。关于这些岩石的起源主要有两种不同的假说：（1）拆沉的下地壳发生部分熔融以及（2）大陆俯冲的上地壳发生部分熔融。虽然大家一致认为地幔中的一些地壳物质已经达到了榴辉岩相，但是仍然证据不足。高 Mg#安山岩样品中 cpx 的反环带显示低 Mg#的核部比高 Mg#的边部具有更低的 Sr 含量和 Sr/Y 比值，这说明母岩浆是由一些榴辉岩衍生的长英质熔体与地幔橄榄岩相互反应而形成的。总体而言，类似地幔的锆石 $\delta^{18}O$ 值（平均值为~ 5.9‰）和 $\varepsilon_{Hf}(t)$值（最高为+6.7）表明其来源为基性岩，而非埋藏的上地壳岩石。由于 EARs 是在地壳缩短结束后的短时间内形成的，长英质熔体极有可能来源于拆沉的榴辉岩化下地壳。这一拆沉过程解释了青藏高原中部早始新世的低起伏地形和无榴辉岩的现今地壳组成。然而，根据各种不同的证据，包括沉积物来源、同位素古海拔和热年代学，地表隆起作为岩石圈拆沉的响应，很可能是可以忽略不计的，这也许是因为青藏高原中部的地壳流变性质较弱。

ABSTRACT: This study used clinopyroxene (cpx) compositions and zircon Hf-O isotopes of Eocene adakitic rocks (EARs) from the Qiangtang block to resolve the mechanism(s) responsible for the formation of the central Tibetan Plateau. The two leading and opposing hypotheses for the origin of these rocks are (1) partially molten foundered lower crust, and (2) partial melting of continentally subducted upper crust. The consensus is that some crustal sources within the mantle have reached eclogite facies, while evidence remains insufficient. Reverse zonation for cpx in high Mg# andesitic samples shows a low Mg# core with lower Sr and Sr/Y than the high Mg# rim, suggesting derivation of parent magma by interaction between some eclogite-derived felsic melts and mantle peridotite. Overall, the mantle-like zircon $\delta^{18}O$ (mean value of ~5.9‰) and $\varepsilon_{Hf}(t)$ (up to +6.7) values argue for a mafic

source rather than buried upper-crustal rocks. Given the EARs were formed within a short time span after the end of crustal shortening, the original felsic melts were most likely derived from the foundered and eclogitized lower crust. The foundering process explains the early Eocene low-relief topography and the intermediate, eclogite-free modern crustal composition of central Tibet. Surface uplift as a response to lithosphere removal, however, was likely negligible, based on various lines of evidence, including sediment provenance, isotope paleoaltimetry, and thermochronology, perhaps because the central Tibetan crust was weak.

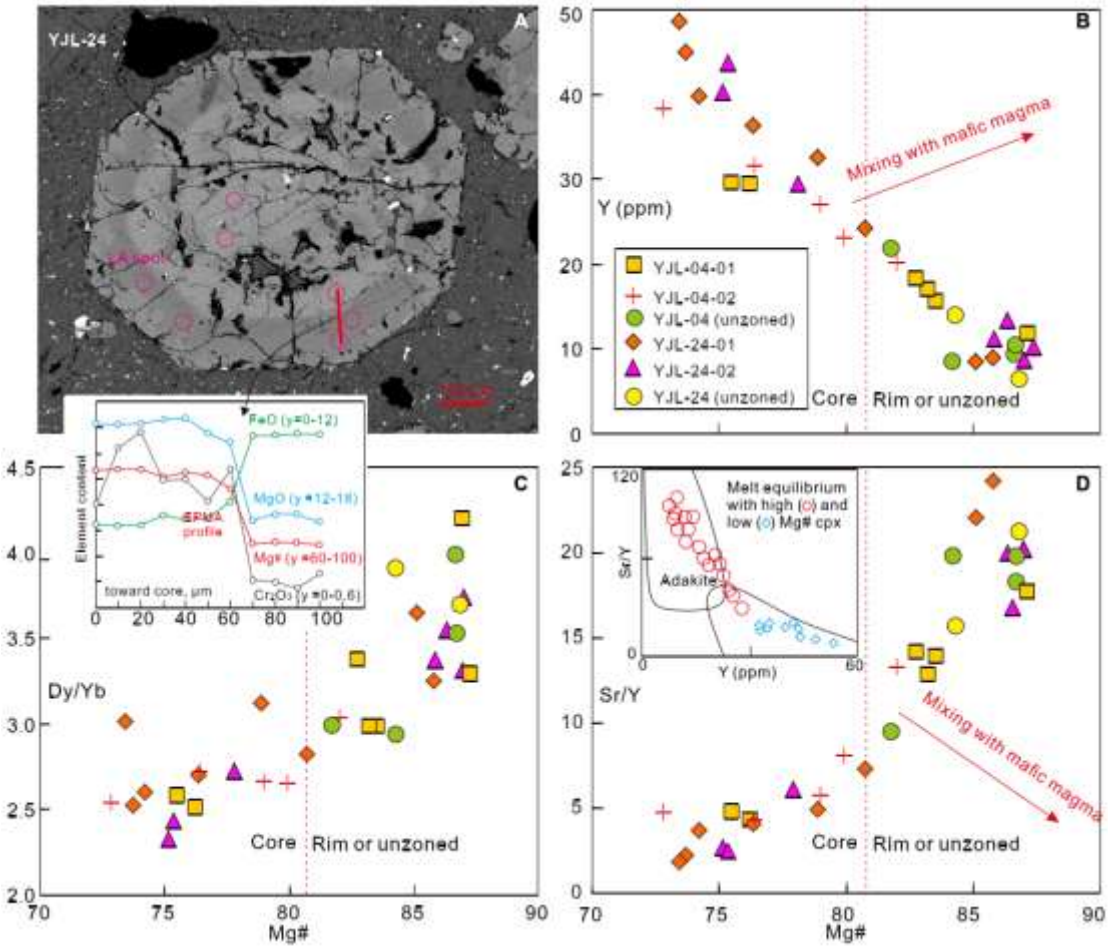

Figure 1. Representative textural (backscattered electron images; see Fig. S2 for photomicrograph [see footnote 1]) and compositional complexities of clinopyroxene (cpx) in primitive Eocene adakitic rocks (EARs). Inset shows composition profile, where values (e.g., MgO [y = 12–18]) refer to range of y axis. LA—laser ablation; EPMA—electron probe microanalysis.

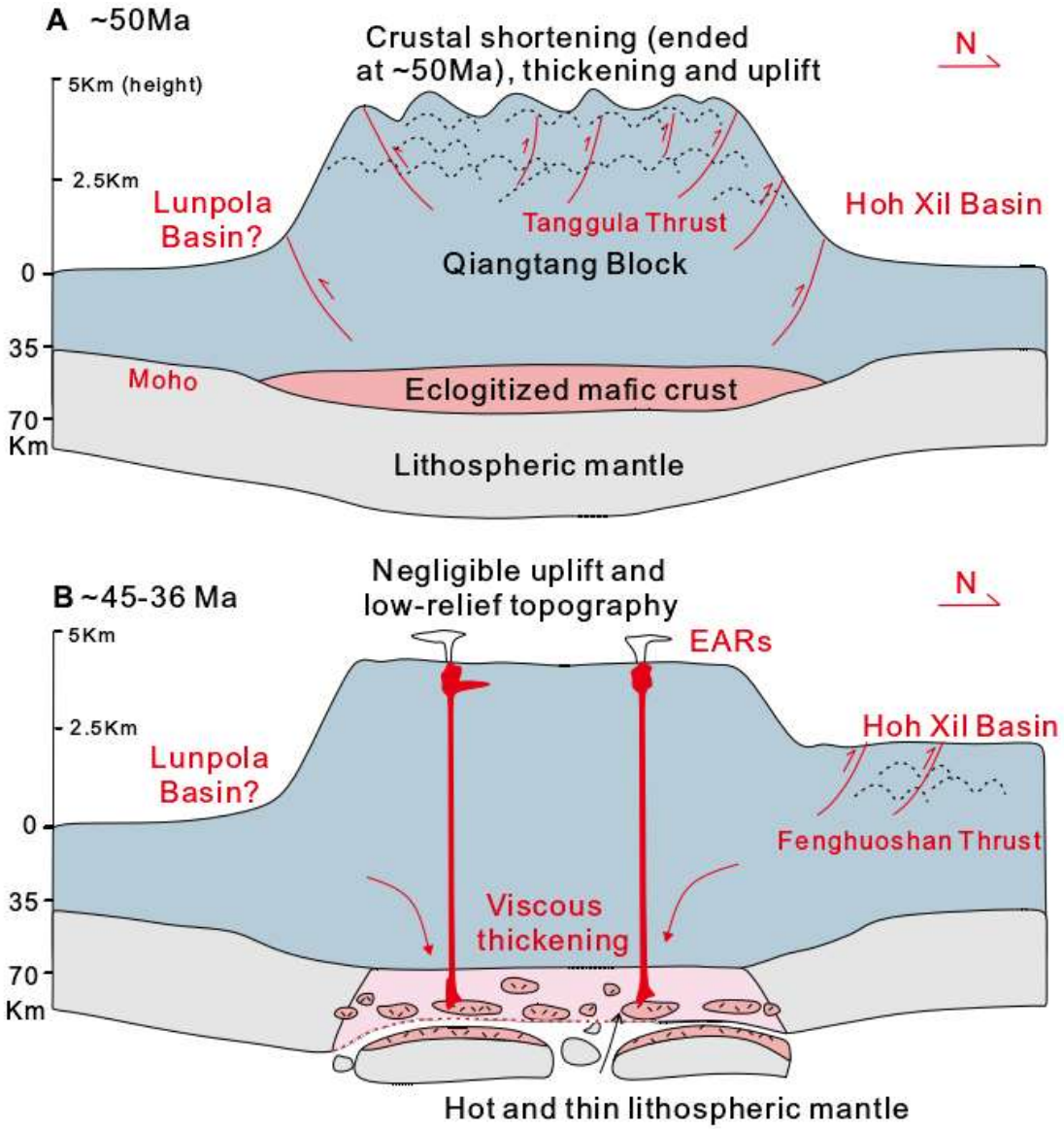

Figure 2. Cartoon illustration of early Paleogene tectono-topographic evolution of central Tibet. Paleo-elevation is based on Xu et al. (2013). EARs—Eocene adakitic rocks.

4. 一个全球洋壳年龄和海底扩张参数的数据库

翻译人:李园洁 liyj3@sustech.edu.cn

Seton, M., Müller, R. D., Zahirovic, S., Williams, S., Wright, N. M., Cannon, J., et al. ***A global dataset of present-day oceanic crustal age and seafloor spreading parameters. Geochemistry, Geophysics, Geosystems****, 2020, 21.*

https://doi.org/10.1029/2020GC009214

摘要：本文展示了最新的洋壳年龄网格化数据和其他补充的数据包括扩张速率，不对称性，方向和倾斜度。文中的数据库基于磁异常识别和 Müller et al. (2019)的板块构造模型。我们发现洋壳的平均年龄为 64.2 Myrs，比之前估计的更古老，主要是由于包含有大量大西洋和地中海中生代的洋壳并改进侏罗纪太平洋三角区。这个较老的洋壳年龄部分被过去模型中未包含的新生代弧后盆地的洋壳年龄抵消。对于现存洋壳的扩张模式的分布，慢速(20-55 mm/yr)和快速(75-180 mm/yr) 扩张系统基本持平，分别占 33%和 39%。中等速率扩张系统(55-75 mm/yr)的洋壳占据 20%，超慢速(5%)和超快速(3%)扩张系统的洋壳只有很小的比例。慢速和中等速率扩张系统在扩张不对称性和倾斜度上表现最稳定，超慢速扩张系统具有最广泛的倾斜，这与现在观测结果一致。我们的置信度网格可为非专业人士提供一个补充资源来识别无需很好约束的年龄网格。在线资源和 GPlates 数据门户免费提供 6、2 和 1 弧分分辨率的网格以及 python 工作流 isopolate 用于计算。

ABSTRACT：We present an updated oceanic crustal age grid and a set of complementary grids including spreading rate, asymmetry, direction and obliquity. Our dataset is based on a selected set of magnetic anomaly identifications and the plate tectonic model of Müller et al. (2019). We find the mean age of oceanic crust is 64.2 Myrs, slightly older than previous estimates, mainly due to the inclusion of pockets of Mesozoic aged crust in the Atlantic and Mediterranean and improvements to the Jurassic Pacific triangle. This older crust is partly compensated by additional Cenozoic‐aged back‐arc basin crust not included in previous models. The distribution of spreading modes based on area of preserved crust is relatively equal between slow (20-55 mm/yr) and fast (75-180 mm/yr) spreading systems at 33 and 39%, respectively. Crust transitional

between fast and slow, or intermediate systems (55-75 mm/yr), cover 20% of the preserved ocean floor with much smaller proportions of crust formed at ultra-slow (5%) and super-fast (3%) spreading systems. Slow and intermediate spreading systems exhibit the most stable behavior in terms of spreading asymmetry and obliquity, with the widest distribution of obliquities occurring at ultra‐slow spreading systems, consistent with present‐day observations. Our confidence grid provides a complementary resource for non‐experts to identify those parts of the age grid that are least well constrained. Our grids in 6, 2 and 1 arc‐minute resolution as well as our python workflow, *isopolate*, used to compute our datasets are freely available in online repositories and on the GPlates data portal.

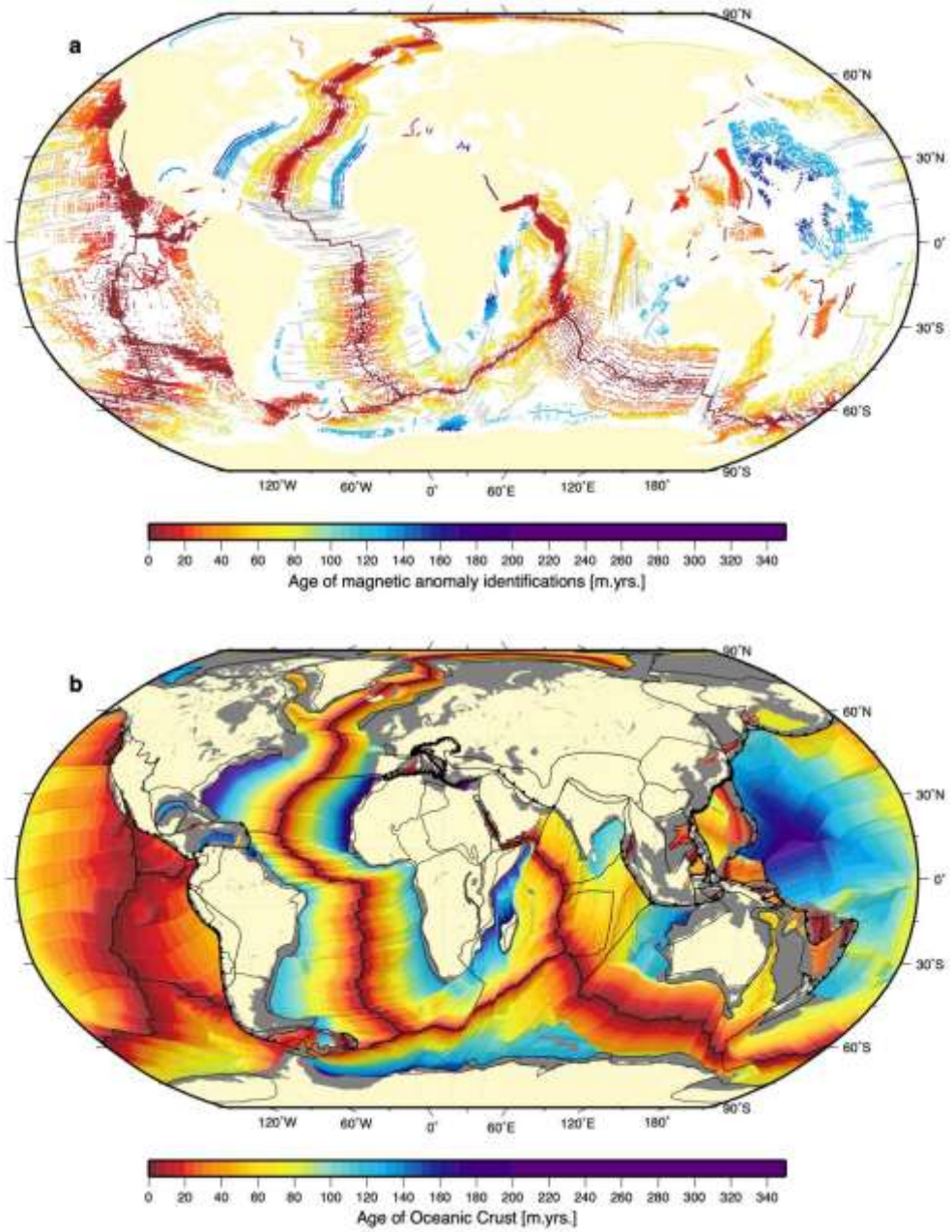

Figure 1. (a.) Constraints used to derive the present-day map of the age of the oceanic crust. These include a preferred magnetic pick compilation (color coded by age) extracted from magnetic anomaly identifications found on the GSFML website (Seton et al., 2014), active and extinct spreading ridges used in the computation of the age grid and a global map of fracture zones and other tectonic fabric (thin grey lines, (Matthews et al., 2011; Wessel et al., 2015)). Robinson projection centered on 30° E. (b.) Resultant present-day grid of the age of the oceanic crust. Present-day plate boundaries are from the global deforming plate model of Müller et al. (2019) with regions of present-day deformation marked as grey polygons.

5. 对 Thellier 方法具有非理想行为样品的加热和微波古强度方法对比

翻译人：柳加波

Grappone, J.M., Biggin, A.J., Barrett, T.J., Hill, M.J., Sprain, C.J., 2020. ***Comparison of Thermal and Microwave Paleointensity Estimates in Specimens Displaying Non‐Ideal Behavior in Thellier‐Style Paleointensity Experiments.*** *J. Geophys. Res. Solid Earth 125.*

https://doi.org/doi:10.1029/2020jb019802

摘要：确定古地磁场强度对理解地核和地球发电机至关重要，但是要获得可靠的古强度值仍然充满挑战。在全球古强度数据库中，0-5 Ma 的磁场强度数据有超过四分之一来自夏威夷。之前两个关于 SOH1 岩芯的研究，明显由于方法的不同，给出了平均差达 30%的古强度差异值。这两项研究中使用的古强度方法在退磁机制（加热或微波辐射）和 Thellier-style 方法（perpendicular and original Thellier protocols）均不同。这两个变量都可能导致估算值的巨大差异。因此，通过结合此前未验证的 thermal-perpendicular 和 microwave-original Thellier 方法，我们对 79 块样品进行古强度实验，从而分析退磁机制和隔离方法的作用。我们发现，单独的退磁机制和方法都不能完全解释古强度估计的差异。具体而言，我们发现基于 original Thellier 方法（独立于退磁机制），增强了非理想的类似多畴状态的效应，通常会导致古强度过高估计。但是，我们也发现证据支持从 1960 年基拉韦厄火山熔岩流获得的最新研究成果，由于不考虑在更高的微波功率下样品的改变，没有 pTRM 检验的 microwave-perpendicular 实验会导致对古强度的低估。总之，这些发现支持真实的古强度介于先前发表的估计值之间，并强调未来的研究（加热或微波）需要同时具有 pTRM 检验和大量检测非理想晶粒作用。

ABSTRACT: Determining the strength of the ancient geomagnetic field is vital to our understanding of the core and geodynamo, but obtaining reliable measurements of the paleointensity is fraught with difficulties. Over a quarter of magnetic field strength estimates within the global paleointensity database from 0 to 5 Ma come from Hawaii. Two previous studies on the SOH1 drill core gave inconsistent, apparently method‐dependent paleointensity estimates, with an average difference of 30%. The paleointensity methods employed in the two studies differed both in demagnetization mechanism (thermal or microwave radiation) and Thellier‐style

protocol (perpendicular and original Thellier protocols)—both variables that could cause the strong differences in the estimates obtained. Paleointensity experiments have therefore been conducted on 79 specimens using the previously untested combinations of thermal - perpendicular and microwave - original Thellier methods to analyze the effects of demagnetization mechanism and protocol in isolation. We find that, individually, neither demagnetization mechanism nor protocol entirely explains the differences in paleointensity estimates. Specifically, we found that non - ideal multidomain - like effects are enhanced using the original Thellier protocol (independent of demagnetization mechanism), often resulting in paleointensity overestimation. However, we also find evidence, supporting recent findings from the 1960 Kilauea lava flow, that microwave - perpendicular experiments performed without partial thermal remanent magnetization checks can produce underestimates of the paleointensity due to unaccounted - for sample alteration at higher microwave powers. Together, these findings support that the true paleointensities fall between the estimates previously published and emphasize the need for future studies (thermal or microwave) to use protocols with both partial thermal remanent magnetization checks and a means of detecting non - ideal grain effects.

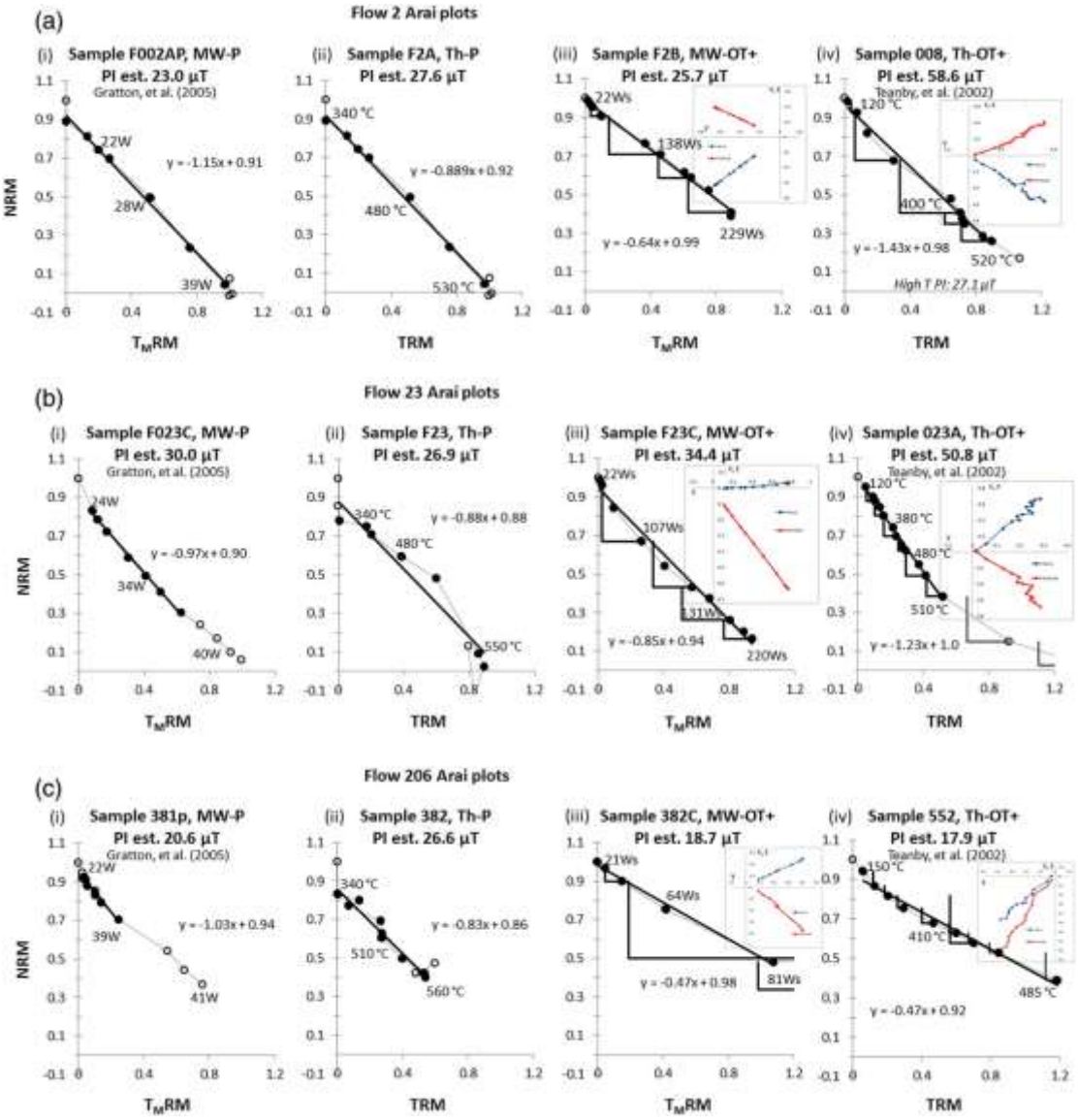

Figure 1: Normalized Arai plot examples comparing the different methods used. (a) Flow 2 (503 - cm thickness), (b) Flow 23 (137 - cm thickness), and (c) Flow 206 (290 - cm thickness). The data are normalized by NRM_0. The filled circles are accepted data points, with the solid black line being the best fit line. Open circles are rejected data points. The black right angle lines are $pT_{(M)}RM$ checks, which are only present in OT+ data. Orthogonal vector plots are provided in core coordinates for the OT+ data. All specimens presented pass their original study's selection criteria. The microwave data are visually more linear than the thermal data, and the OT+ data are often two - sloped. The powers given for the Gratton et al. (2005) MW data are power applied and the power integrals given in the new data are (inferred) energy absorbed.

6. 微量金属元素作为古环境指标---为什么我们要考虑沉积速率的变化?

翻译人：刘伟 inewway@163.com

Crombez V , Rohais S , Euzen T , et al. ***Trace metal elements as paleoenvironmental proxies: Why should we account for sedimentation rate variations?****[J]. Geology, 2020.48 (8): 839–843.*

https://doi.org/10.1130/G47150.1

摘要：微量金属元素(TMEs)通常用于重建富有机质沉积物沉积过程中的古环境条件。例如，由初级生产力变化和氧化还原条件控制的 TME 浓度被广泛应用于古环境研究。最近，这些 TMEs 指标重新引起了人们的兴趣，并普遍用于大尺度(10-1000 公里)的研究。然而，在盆地尺度上应用这些地球化学指标而忽略沉积速率的变化可能导致错误的古环境重建。在这里，我们展示了沉积速率（SR）如何影响地球化学记录，并可能导致对 TMEs 演化的错误解释。在考虑 SR 的基础上，计算了加拿大西部三叠系 Upper Montney 组和 Doig Phosphate 组 TMEs 的自生组分累积速率（AFAR），并对阿根廷侏罗系白垩纪 Vaca-Muerta 组 TMEs 的 AFAR 进行了修正。相对于传统的 TME 结果，SR 校正的 TME 结果需要对古环境进行不同的解释，并强调了通常被解释为缺氧沉积环境的指示，可能反映了低 SR 和凝缩段的形成。这项工作还引入了一个新的工作流程，即在盆地尺度和长时间尺度的古环境研究中考虑 SR。

ABSTRACT: Trace metal elements (TMEs) are commonly used to reconstruct the environmental conditions present during the deposition of organic-rich sediments. For example, TME concentrations controlled by changes in primary productivity and redox conditions are widely used in paleoenvironmental studies. Recently, these proxies have undergone a resurgence of interest and are commonly used in large-scale (10–1000 km) studies. However, applying these geochemical proxies at basin scale while ignoring variations in sedimentation rates (SR) may lead to misinterpretation of paleoenvironmental conditions. Here, we show how SR can affect the geochemical records and may lead to incorrect interpretations of TME evolution. Accounting for SR, we computed the authigenic fraction accumulation rates of key TMEs in the Upper Montney Formation and Doig Phosphate (Triassic, western Canada), and we correct the concentration of these elements in the Vaca-Muerta

Formation (Jurassic–Cretaceous, Argentina). Our SR-corrected TME proxies require a different interpretation of paleoenvironmental conditions (e.g., primary productivity, basin restriction) compared to conventional TME results and highlight that elementary enrichments commonly interpreted as indicative of anoxic depositional environments may reflect low SR and the formation of condensed intervals. This work also introduces a new workflow to account for SR in paleoenvironmental studies at basin scale and over long time periods.

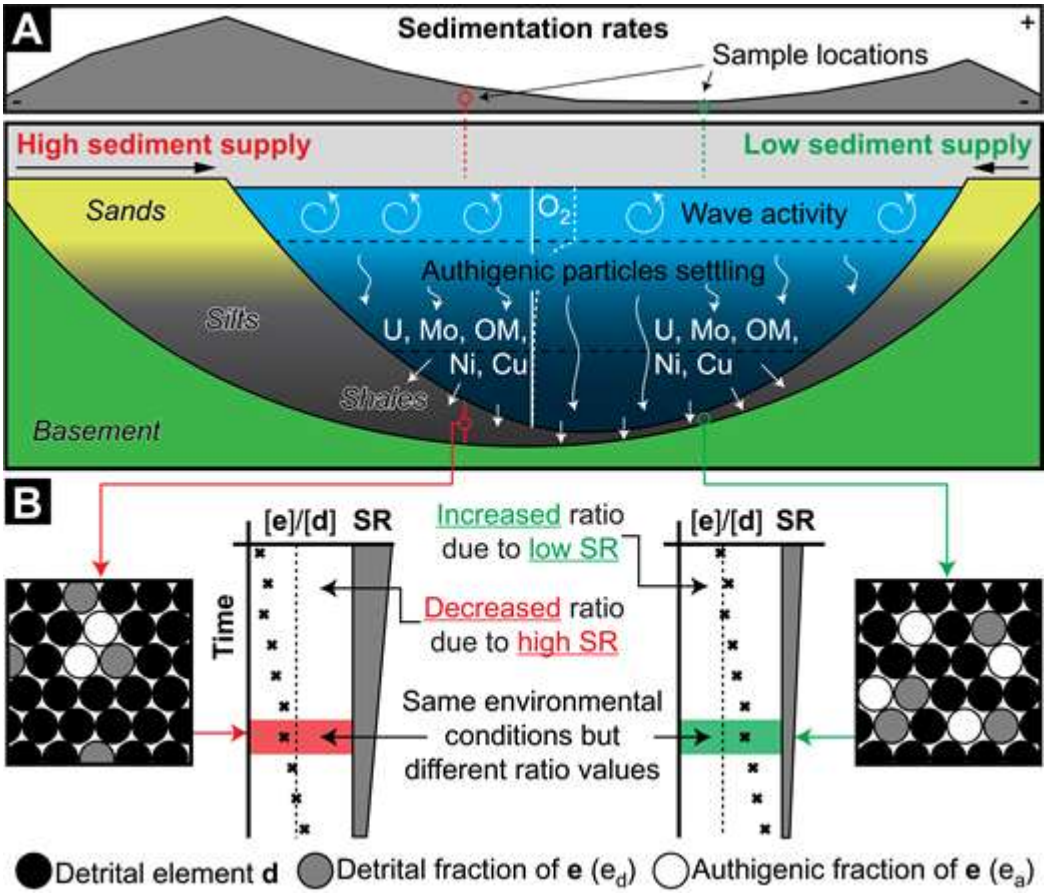

Figure 1. Influence of different sedimentation rates on concentration of authigenic elements. (A) Conceptual basin where sediment supply at each margin is different. (B) Variations in dilution of authigenic elements in two locations, each related to different sediment supplies. OM—organic matter; SR—sedimentation rate.

7. 白垩纪高北极地区海洋的形成

翻译人：曹伟 11930854@QQ.com

A. Døssing, C. Gaina, H.R. Jackson, et al., ***Cretaceous ocean formation in the High Arctic.*** *[J]. Earth and Planetary Science Letters, 2020(551): 116552*

https://doi.org/10.1016/j.epsl.2020.116552

摘要：了解海盆的演化对于研究全球板块构造、地幔动力学、海平面变化和识别板块构造边界具有非常重要的作用。由于白垩纪高北极地区大火成岩省的广泛覆盖，北冰洋 250 万平方公里的 Amerasia 盆地的演化过程仍然没有定论。在 Amerasia 盆地南部（位于加拿大盆地）发现了一个已经死亡但埋藏较深的扩张中心（此处为 South Amerasia Ridge, SAR）。然而，SAR 的结构细节以及加拿大盆地的动态演化仍然有待解决。基于最新卫星重力模型进行三维反演和垂向梯度研究，我们获取到加拿大盆地扩张系统中的新构造，并且该研究结果得到了航磁分析和近期海洋地球物理数据的支持。结果表明，SAR 扩张中心呈现出一致的阶梯状右向倾斜切分，扩张段被整个洋壳都可追踪到的东北向非转换断层抵消，并与加拿大盆地较老部分的古洋壳走滑断层平行。我们认为 SAR 是由东北-西南方向的高度倾斜扩张形成。我们将预测的 SAR 基底地形与全球洋脊系统进行比较，得到了同样受基底地形约束的详细磁模型。结果表明，SAR 地壳形成于一个缓慢到中速的扩展机制，海底扩张在磁极反转时期结束，很可能在早白垩世。我们的新板块重建模型采用了加拿大盆地的高度倾斜扩张，需要 Alaska/Chukotka 构造块体的平移运动，取代了白垩纪高北极地区数十年前的旋转模式。

ABSTRACT: Understanding the evolution of ocean basins is critical for studies in global plate tectonics, mantle dynamics, and sea-level through time, and relies on identifiable tectonic plate boundaries. The evolution of the 2.5 million km^2 Amerasia Basin in the Arctic Ocean remains largely unsettled due to widespread overprint by the Cretaceous High-Arctic Large Igneous Province. Traces of an extinct, but deeply buried, spreading centre (herein South Amerasia Ridge, SAR) has been shown to exist in the southern part of the Amerasia Basin, in the Canada Basin. However, structural details of the SAR and, hence, the kinematic evolution of the Canada Basin, are yet to be unraveled. Based on 3D gravity inversion and the vertical gravity gradient of the

latest generation of satellite gravity models, we document new structures within the Canada Basin spreading system. Our results are supported by analysis of aeromagnetic and recent marine geophysical data. Evidence is shown of consistent oblique segmentation of the SAR spreading centre in a right stepping en echelon pattern. The spreading segments are offset by northeast-trending non-transforms that are traceable throughout the oceanic crustal domain and parallel to pre-oceanic strike-slip faults in the older part of the Canada Basin. We interpret the SAR to have formed by highly oblique spreading in a northeast-southwest direction. We compare the predicted SAR basement topography with the global ridge systems and produce a detailed magnetic modelling also constrained by the basement topography. The results indicate that the SAR crust formed by a slow-to-intermediate spreading regime and that sea-floor spreading terminated during a reverse polarity chron, most likely in the Early Cretaceous. Our novel plate reconstruction model, adopting a highly oblique spreading in Canada Basin, requires a translational motion of the Alaska/Chukotka tectonic block, replacing the decades-old rotational model of the Cretaceous High Arctic.

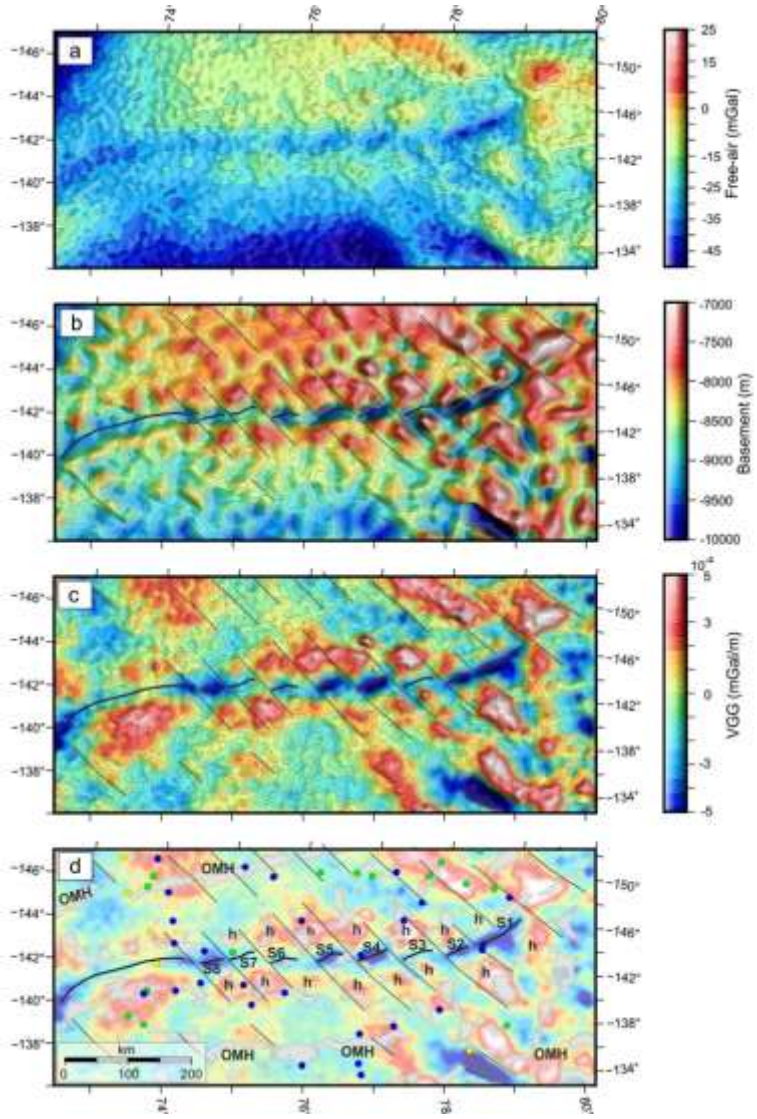

Figure 1. SAR morphology analysis. (a) DTU15 free-air gravity. (b) Basement topography derived from 3D gravity inversion. (c) VGG of free-air anomalies. (d) VGG combined with crustal information of from seismic sonobuoy analysis (Chian et al., 2016) and filled (grey) the 0.7 radian contour of the magnetic tilt derivative.

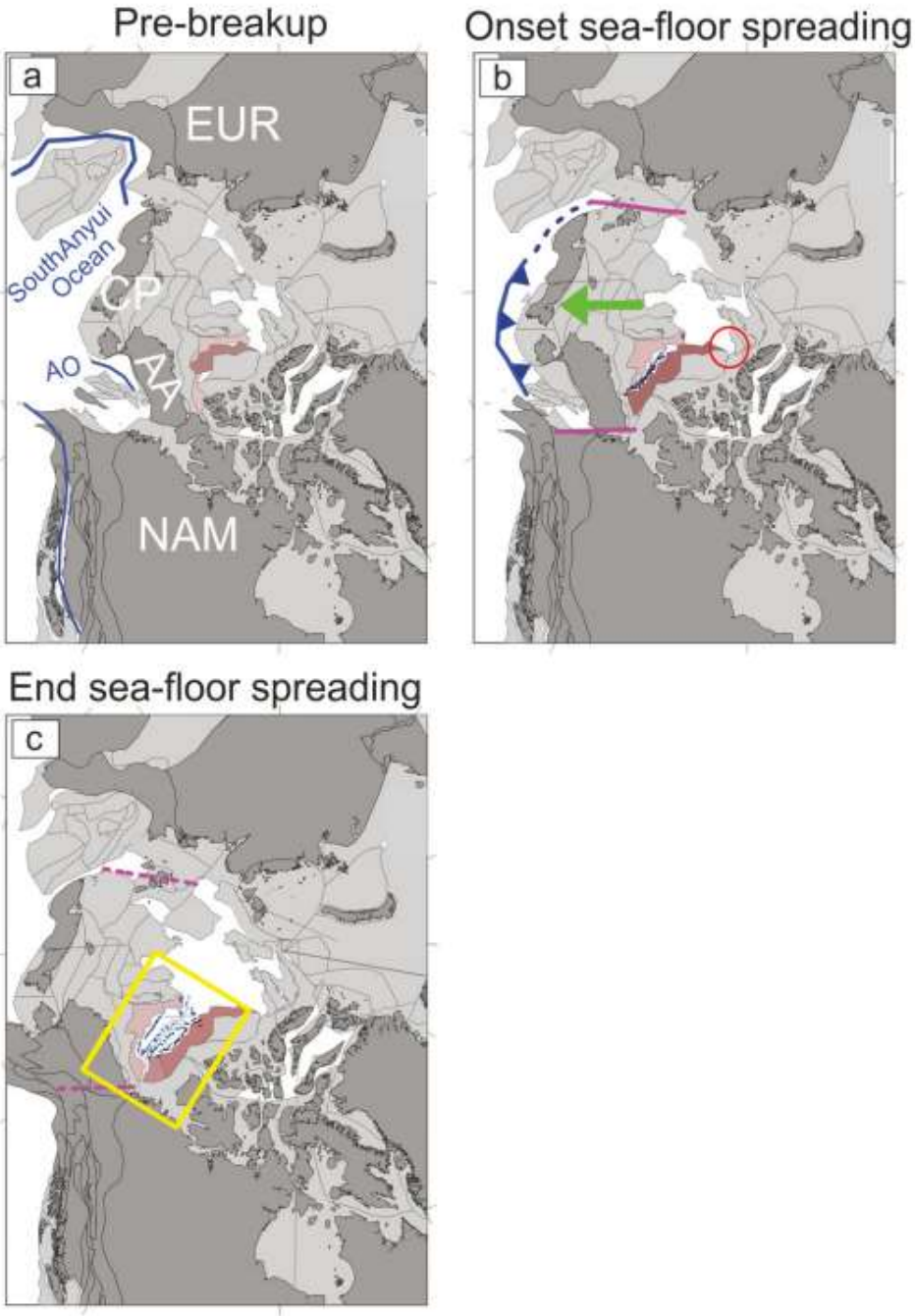

Figure 2. (a) Pre-breakup scenario; (b) Onset of sea-floor spreading; (c) End of sea-floor spreading. Blue curves: location of trenches; Green arrow: motion of Alaska (AA) - Chukotka (CP) microplate; Magenta lines: approximate location of transform fault zones; Red circle: approximate location of a mantle plume that created the High Arctic Large Igneous province (HALIP).

8. 亚洲夏季风：遥相关与驱动机制——中国石笋记录综述

翻译人：杨会会 11849590@mail.sustech.edu.cn

Zhang H W, Brahim Y A, Li H Y et al., The Asian Summer Monsoon: Teleconnections and Forcing Mechanisms—A Review from Chinese Speleothem $\delta^{18}O$ Records [J]. Quaternary, 2019,2,26

https://doi.org/10.3390/quat2030026

摘要：亚洲夏季季风(ASM)的变化显著影响着东亚地区的水文气候，也影响着东亚地区居住的全球近三分之一人口的社会经济。在过去的二十年里，利用来自中国的石笋 $\delta^{18}O$ 记录，重建了 ASM 的变化及其在轨道尺度至季节尺度的潜在驱动机制。本文利用石笋同位素合成与分析数据库(SISAL_v1)，对亚洲季风在晚更新世、全新世和最近两千年的水文气候变化进行了综述。我们强调了在不同的时间尺度上，ASM 可能存在的全球遥相关和驱动机制。最长的覆盖了过去 640 kyr BP 的石笋 $\delta^{18}O$ 合成记录表明，在轨道时间尺度上，ASM 的变化主要是由 23 kyr 岁差周期决定，与北半球的夏季日照是相一致。在末次冰期，ASM 在千年尺度上的变化似乎受到北大西洋气候和海洋反馈的控制。在全新世，ASM 强度的变化主要受 NHSI 控制。然而，季风雨带的时空分布在十年到千年的时间尺度上可能会随着 ASM 强度变化而变化。

Abstract: Asian summer monsoon (ASM) variability significantly affects hydro-climate, and thus socio-economics, in the East Asian region, where nearly one-third of the global population resides. Over the last two decades, speleothem $\delta^{18}O$ records from China have been utilized to reconstruct ASM variability and its underlying forcing mechanisms on orbital to seasonal timescales. Here, we use the Speleothem Isotopes Synthesis and Analysis database (SISAL_v1) to present an overview of hydro-climate variability related to the ASM during three periods: the late Pleistocene, the Holocene, and the last two millennia. We highlight the possible global teleconnections and forcing mechanisms of the ASM on different timescales. The longest composite stalagmite $\delta^{18}O$ record over the past 640 kyr BP from the region demonstrates that ASM variability on orbital

timescales is dominated by the 23 kyr precessional cycles, which are in phase with Northern Hemisphere summer insolation (NHSI). During the last glacial, millennial changes in the intensity of the ASM appear to be controlled by North Atlantic climate and oceanic feedbacks. During the Holocene, changes in ASM intensity were primarily controlled by NHSI. However, the spatial-temporal distribution of monsoon rain belts may vary with changes in ASM intensity on decadal to millennial timescales.

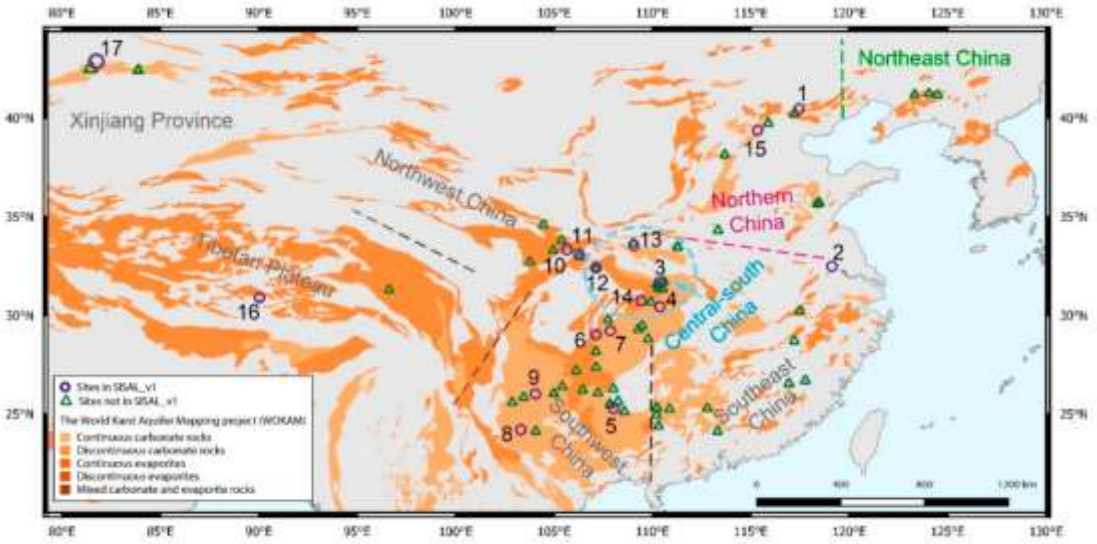

Figure 1. Map showing the location of speleothem records in China, superimposed on a map showing the distribution of carbonate and evaporite rocks provided by the World Karst Aquifer Mapping Project (WOKAM [30]). Purple circles indicate cave sites with speleothem records that are available in SISAL_v1 [18] (1: Kulishu; 2: Hulu; 3: Sanbao; 4: Heshang; 5: Dongge; 6: Yangkou; 7: Furong; 8: Xiaobailong; 9: Zhuliuping; 10: Huangye; 11: Dayu; 12: Suozi; 13: Jiuxian; 14: Xinya; 15: Xinglong; 16: Tianmen; 17: Kesang). Green triangles show cave sites identified, but not included in SISAL_v1.Specific information on sites, entities, and references is given in Table 1.

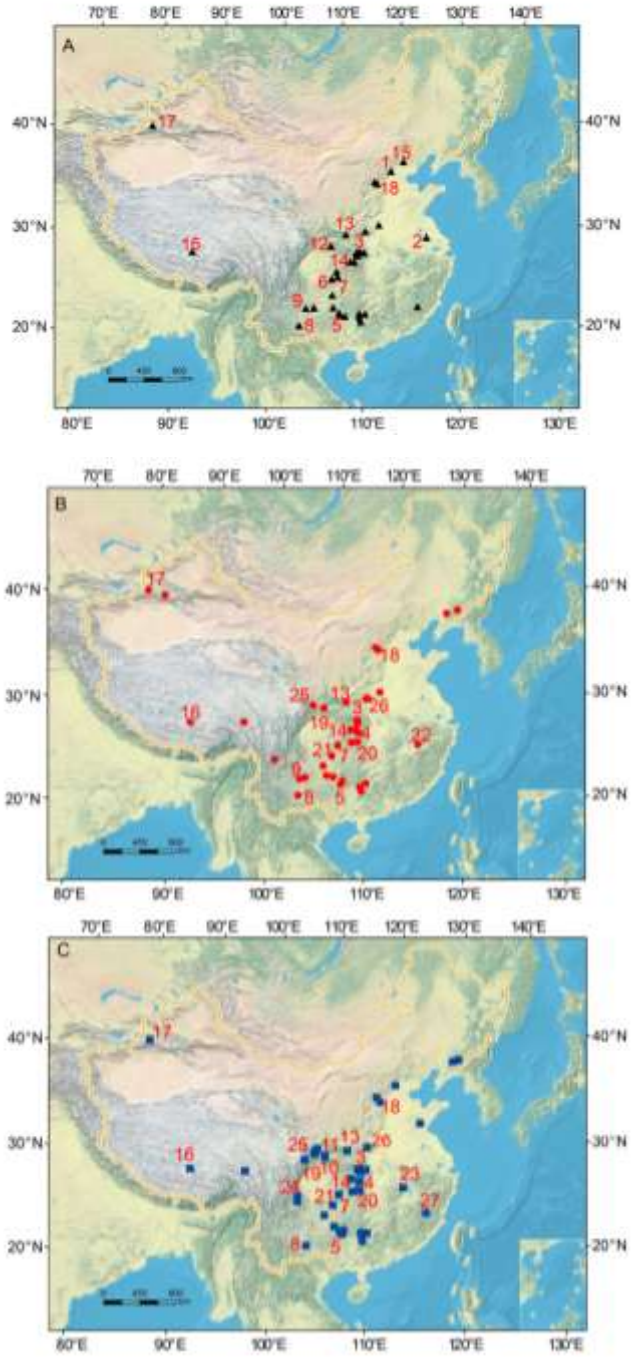

Figure 2. Spatial distribution of speleothem $\delta^{18}O$ records in China during three periods: (A) the Late Pleistocene (640 ka–11.7 ka), (B) the Holocene (11.7 ka–Present), and (C) the last 2000 years. Cave locations numbered 1–17 are the same as in Figure 1. Numbers 18–27 (18: Lianhua (Shanxi); 19: Xianglong; 20: Lianhua (Hunan); 21: Shigao; 22 Shennong; 23: E'mei; 24: Shenqi; 25: Wanxiang; 26: Dongshiya; 27: Yuhua) are records mentioned in the discussion but not in SISAL_v1. Details on each speleothem are given in Table 1.

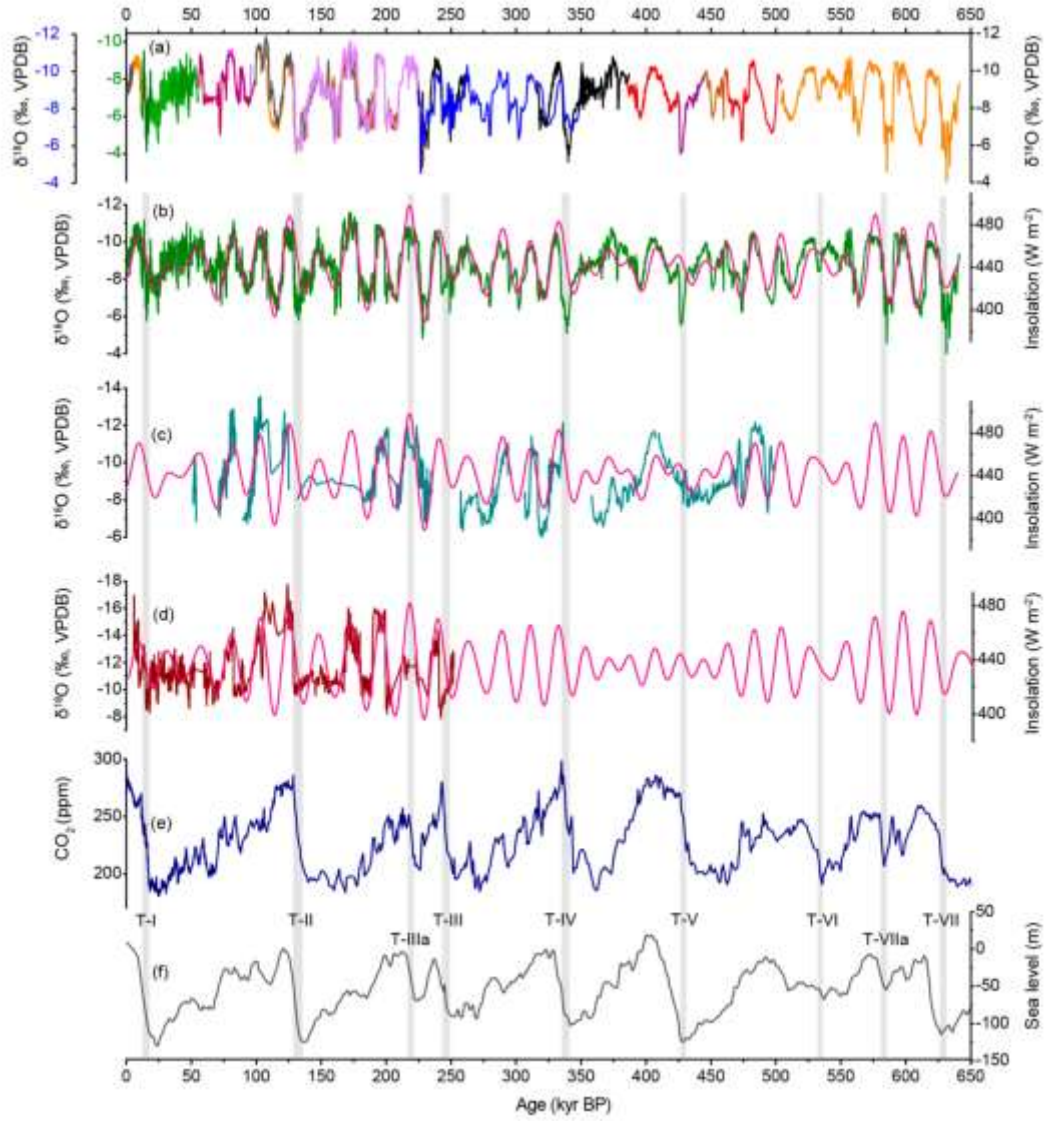

Figure 3. Orbital scale changes in speleothem $\delta^{18}O$ records from China and comparison with other records. (A) Multi-speleothem record from China: three records from the Hulu Cave (green curves; green left *y*-axis), two records from the Linzhu Cave (blue curves; blue left *y*-axis), and 16 records from the Sanbao Cave (all other colors; black right *y*-axis). (B) The 640 kyr EASM composite record from (A) [1]. (C) The composite $\delta^{18}O$ record from the Kesang Cave (cyan curve) [21]. (D) The composite $\delta^{18}O$ record from the Xiaobailong Cave (brown curve) [13]. Pink curves in panels B–D show 21 July insolation at 65° N [206]. (E) The composite CO_2 record [207]. (F) The composite sea level record [208]. Vertical gray bars mark the timing of seven glacial terminations, which correspond with weak monsoon intervals.

9. 始新世-渐新世气候过渡时期的全球碳循环扰动

翻译人：王敦繁 dunfan-w@foxmail.com

Armstrong McKay, D. I., T. Tyrrell, and P. A. Wilson (2016), ***Global carbon cycle perturbation across the Eocene-Oligocene climate transition, Paleoceanography,*** *31, 311–329, doi:10.1002/2015PA002818.*

摘要：始新世-渐新世过渡期(EOT 约 34 Ma)标志着新生代从长期温室气候到冰期气候过渡的一个转折点。古记录显示，在整个 EOT 阶段，气候逐步快速的冷却和冰的增长与底栖有孔虫 ^{13}C 偏移及碳酸盐补偿深度(CCD)的加深紧密相关。基于生物地球化学模型，Merico et al.(2008)提出(1)冰期海平面下降导致的陆架-盆地碳酸盐岩埋藏分馏作用和(2)陆架碳酸盐岩风化作用可以解释碳循环的扰动，但这一发现受到了质疑。备选机制包括增加海洋通风，减少碳酸盐埋藏，增加有机碳埋藏，增加硅酸盐风化和增加海洋钙浓度。在这里，我们使用 Merico 等人(2008)的生物地球化学模型的改进版本来重新评估这些相互竞争的假设和一个额外的机制，即“碳库”的扩展，如永久冻土和泥炭地。我们发现，钙浓度、硅酸盐风化、碳酸盐或有机碳埋藏的变化，都产生了与古记录的形式和/或标志根本不一致的反应。冰架-盆地碳酸盐岩埋藏分馏(CCD 变化)，加上冰架碳酸盐岩风化，将富含 ^{12}C 的碳封存到碳库中，以及可能增加的海洋通风(约 ^{13}C 偏移)，提供了最适合古记录的条件。需要进一步的工作来理解为什么 EOT 碳循环扰动是如此独特，而假设的强迫机制(冷却和冰的生长)不是这个事件所特有的。

ABSTRACT: The Eocene-Oligocene transition (EOT), ~34 Ma, marks a tipping point in the long-term Cenozoic greenhouse to icehouse climate transition. Paleorecords reveal stepwise rapid cooling and ice growth across the EOT tightly coupled to a transient benthic δ13C excursion and a major and permanent deepening of the carbonate compensation depth (CCD). Based on biogeochemical box modeling, Merico et al. (2008) suggested that a combination of (1) glacioeustatic sea level fall-induced shelf-basin carbonate burial fractionation and (2) shelf carbonate weathering can account for the carbon cycle perturbation, but this finding has been questioned. Alternative proposed mechanisms include increased ocean ventilation, decreased carbonate burial, increased organic carbon burial, increased silicate weathering, and increased

ocean calcium concentration. Here we use an improved version of the biogeochemical box model of Merico et al. (2008) to reevaluate these competing hypotheses and an additional mechanism, the expansion of "carbon capacitors" such as permafrost and peatlands. We find that changes in calcium concentration, silicate weathering, and carbonate or organic carbon burial each yield a response that is fundamentally at odds with the form and/or sign of the paleorecords. Shelf-basin carbonate burial fractionation (CCD change), plus shelf carbonate weathering, sequestration of ^{12}C-enriched carbon into carbon capacitors, and possibly increased ocean ventilation (δ13C excursion), offers the best fit to the paleorecords. Further work is needed to understand why the EOT carbon cycle perturbation is so unique when the forcing mechanisms hypothesized to be responsible (cooling and ice growth) are not peculiar to this event.

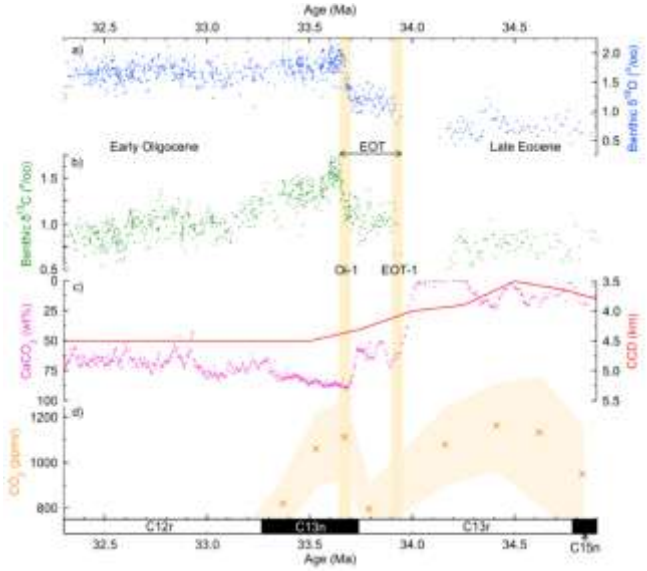

Figure 1. Paleorecords across the Eocene-Oligocene transition (EOT). (a) Benthic δ18O from ODP Site 1218 (8°53′N, 135°22′ W in the equatorial Pacific) (blue) [Coxall and Wilson, 2011], (b) benthic δ13C from ODP Site 1218 (green) [Coxall and Wilson, 2011], (c) the long-term behavior of the CCD in the equatorial Pacific (red line) [Pälike et al., 2012] and CaCO3 wt % from IODP Site 1218 as a qualitative proxy for CCD deepening in the equatorial Pacific (purple dots) [Coxall et al., 2005; Coxall and Wilson, 2011] (using the age model of Westerhold et al. [2014]), and (d) atmCO2 reconstructed from the boron isotope pH proxy (orange crosses, shaded band for uncertainty) [Pearson et al., 2009] between the late Eocene and the early Oligocene. The EOT-1 and Oi-1 cooling and glaciation steps are indicated by the yellow bars, and the Geomagnetic Polarity Timescale [Ogg and Smith, 2004] is shown along the bottom axis.

10. 晚更新世期间气候所导致的地中海向北大西洋的外流

翻译人：王浩森 11930841@mail.sustech.edu.cn

Nichols M D, Xuan C, Crowhurst S, et al. 2020. ***Climate-Induced Variability in Mediterranean Outflow to the North Atlantic Ocean During the Late Pleistocene. 35: e2020PA003947.***

https://doi.org/10.1029/2020PA003947

摘要：地中海外流（MOW）增加了开放大洋中层水的盐分和密度，因此是大西洋经向翻转环流（AMOC）和气候多变性的重要动力。然而，在地质时间尺度上，针对 MOW 的强度和深度变化的文献很少。本文提供了新的详细记录，是 IODP 339 航次从西伊比利亚边界回收的快速积累的海洋沉积物，其精确的年龄是从 416 ka 到现在的 MOW 变化。XRF 测得的物理粒度和磁化率（AMS）各向异性反映古水流的结果表明（i）AMS 理论轴的方向与冰期-间冰期之间的存在着密切的关系，并且（ii）在过去的 416 ka 里，两种不同的 MOW 行为在粒径和 AMS 的变化在轨道和亚轨道上。在 MIS 10 和 MIS 4 之间，MOW 集中在西伊比利亚边缘的一个较浅的深度上，MOW 强度的变化受到岁差的强烈影响。当 MOW 变深并且千年尺度上的流动强度变化叠加在轨道上的变化时，即在 MIS 5 和 MIS 4 期间发生了过渡。在 MIS 11 和从 MIS 3 到现在的时间里，MOW 被重点关注并且记录了千年尺度上的变化。我们推断，MOW 强度和深度在晚更新世的变化被气候强烈影响着，而地中海周围降雨气候的变化可能是主要的控制因素。

ABSTRACT: Mediterranean Outflow Water (MOW) adds salt and density to open ocean intermediate waters and is therefore an important motor of Atlantic meridional overturning circulation (AMOC) and climate variability. However, the variability in strength and depth of MOW on geological timescales is poorly documented. Here we present new detailed records, with excellent age control, of MOW variability from 416 ka to present from rapidly accumulated marine sediments recovered from the West Iberian Margin during Integrated Ocean Drilling Program (IODP) Expedition 339. Our records of X‐ray fluorescence (XRF), physical grain size, and paleocurrent information from the anisotropy of magnetic susceptibility (AMS) indicate (i) a

close relationship between the orientation of principle AMS axes and glacial‐interglacial cycles and (ii) two distinct regimes of MOW behavior over the last ~416 kyr in grain‐size and AMS variability at orbital (mainly precessional) and suborbital timescales. Between marine isotope stage (MIS) 10 and MIS 4, MOW was focused at a generally shallow depth on the West Iberian Margin, and changes in MOW strength were strongly paced by precession. A transition interval occurred during MISs 5 and 4, when MOW deepened and millennial‐scale variability in flow strength was superimposed on orbitally paced change. During MIS 11 and from MIS 3 to present, MOW was deeply focused and millennial‐scale variability dominated. We infer that late Pleistocene variability in MOW strength and depth were strongly climate influenced and that changes in circum Mediterranean rainfall climate were likely a primary control.

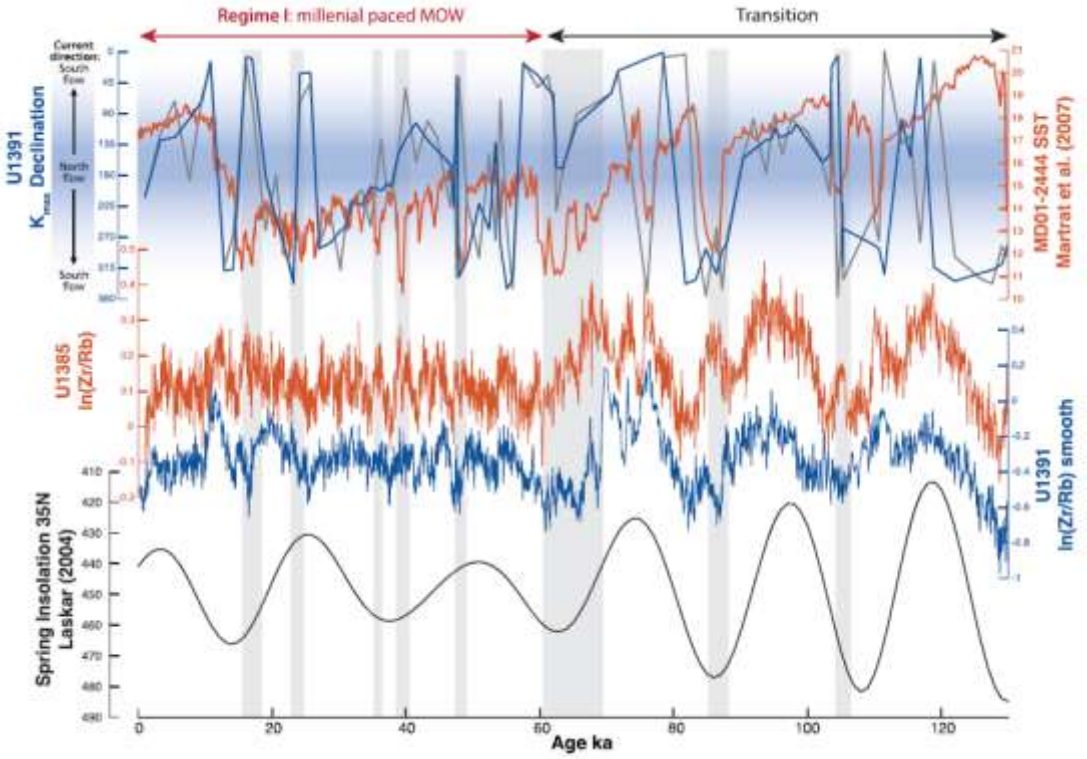

Figure 1. MOW variability during the transition interval and Regime I. From top to the bottom: U1391 K_{max} declination (gray = raw; blue = 3‐point moving average), MD01‐2444 sea surface temperatures (Martrat et al., 2007; orange), ln (Zr/Rb) from Sites U1391 (blue) and U1385 (orange), and spring insolation at 35 ºN (Laskar, 2004; black). Cold events are marked by gray bars.

11. 用水文模型解释东亚季风的湖态记录

翻译人：郑威　11930589@mail.sustech.edu.cn

Yu G, Ye L, Liu Z, et al. ***Interpreting the lake-status record of the East Asian monsoon using a hydrological model****[J]*. ***Quaternary Research****, 1-16.*

https://doi.org/10.1017/qua.2020.63

摘要：东亚季风在过去一万年里变化多端，影响了东亚的农业发展。然而，由于各个湖泊记录的不确定性和全新世中期东亚季风降水模拟的巨大变化限制，在6千年时的东亚季风降水波动的强度和范围仍为解决。我们在这里展示了一个基于多个湖水位记录的方法，使用1D湖水位-2D湖面积-3D流域水文模型来重建中国北部的降水模式，并且进一步量化相较于现在全新世中期东亚季风降水扩张的程度。重建结果显示，东亚季风降水在6千年时向北扩张了约550到1100千米，并向西移动了530到840千米。在那时，东亚季风降水润泽了超过六百万平方公里的土地。因此，这个方法减少了东亚季风降水重建的不确定性和随机性，为未来的气候模型研究提供了基准。

ABSTRACT: The East Asian monsoon (EAM) has experienced significant changes over the past 10,000 years that influenced East Asian agricultural development. However, the magnitude and extent of the EAM precipitation fluctuations at 6 ka remain unresolved, owing to uncertainty in individual lake records and substantial variations in the expansion limits in simulations of the mid-Holocene EAM precipitation. Here we present an approach based on multiple lake-level records using the "1D lake level—2D lake area—3D catchment hydrology" model to reconstruct the precipitation patterns in northern China, and to further quantify the extent of the EAM precipitation expansion in the mid-Holocene relative to today. The precipitation reconstructions suggest an ~550–1100 km northward expansion and an ~530–840 km westward migration of the EAM at 6 ka. At that time, the EAM precipitation domain covered over 6 million square kilometers. Thus, this approach mitigates the

uncertainty and arbitrariness of reconstructions of the limit of the EAM precipitation fields and provides a benchmark for future climate modeling studies.

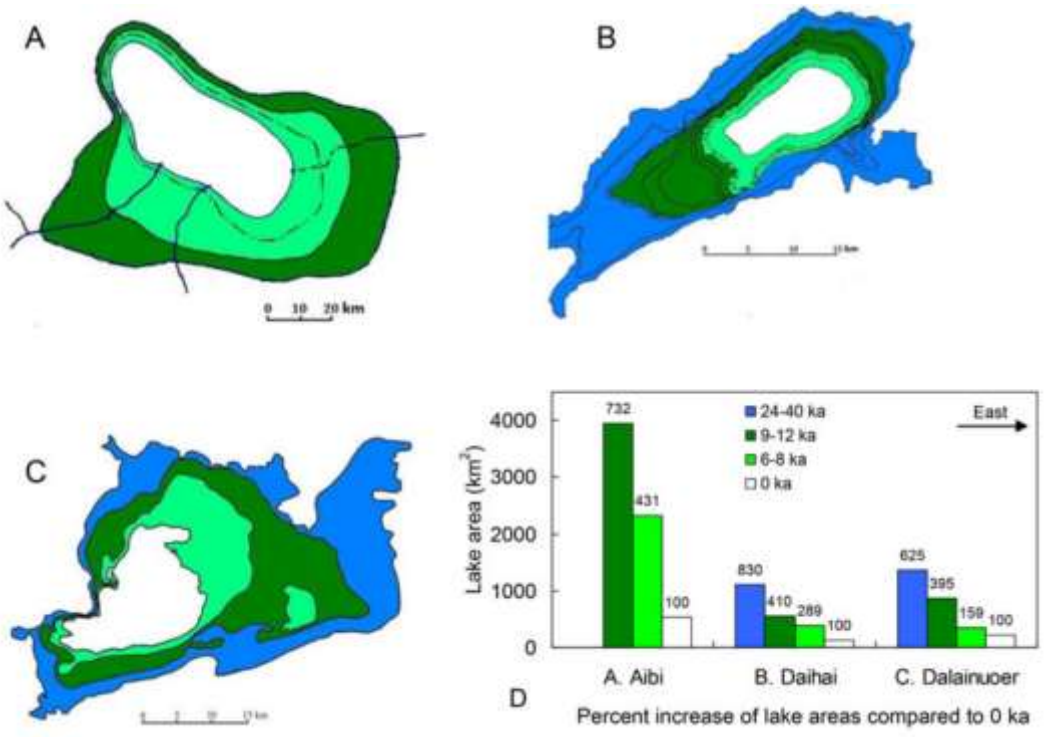

Figure 1. Reconstructions of lake areas at (A) Lake Dalainuoer, (B) Daihai, and (C) Aibi and Percent increase of lake areas during various geological periods compared to 0 ka (D). Lake areas are shown for different time slices: 6–8 ka (green), 9–12 ka (dark green), and 25–40 ka (navy blue); modern water area is in white. (For interpretation of the references to color in this figure legend, the reader is referred to the web version of this article.)

12. 低磁性基岩地区红壤中纳米磁铁矿聚集体从源到汇迁移过程中的变化及古气候意义

翻译人：张伟杰 12031188@mail.sustech.edu.cn

Zhang Q, Appel E, Hu S, Pennington RS, Meyer J, et al. 2020. ***Nano-magnetite aggregates in red soil on low magnetic bedrock, their changes during source-sink transfer and implications for paleoclimate studies****. Journal of Geophysical Research: Solid Earth*

https://doi.org/10.1029/2020JB020588

摘要：土壤与湖泊沉积物是重要的古环境记录，经常构成源-汇体系。为了更好的理解从源到汇过程中磁学性质的变化，本文研究了鹤庆盆地低磁性基岩之上的红壤与草海的近代沉积物。本地区的红壤磁化率较高~$10^{-5}m^3/kg$,是草海沉积物仅有的重要物源。红壤中的磁性矿物主要是成土过程中形成的纳米磁铁矿颗粒（~10-15nm）的聚集体（~100nm），纳米磁铁矿颗粒的相互作用引起了磁性颗粒有效粒径从超顺磁到稳定稳定单畴广泛分布。透射电子显微镜与宽频率磁化率显示了在红壤的物质向草海迁移过程中聚集体颗粒分解及纳米颗粒向赤铁矿变化的增加。磁性颗粒的磁畴状态向更小的有效粒径的转变导致了更低的 χ_{fd}%、χ 以及 χ(f) 的特征变化。红壤中磁性颗粒聚集体 SP-SSD 的分布可能与气候相关，饱和等温剩磁与磁化率的比值是一个有潜力的反映基岩特征的气候指标。草海沉积物的磁学性质主要受到纳米磁铁矿聚集体与基岩来源的大颗粒磁铁矿影响。本研究结果与之前在鹤庆盆地研究的长 168m 岩心(900-30 ka)的古气候解释不同。单独的磁铁矿纳米颗粒不消失，只有磁铁矿聚集体的分散也可能产生具有较低的频率磁化率的 SP 行为，根据频率磁化率得到的 SP 磁铁矿溶解的假设可能是有问题的。

ABSTRACT: Soil and lake sediments are important paleoclimate archives often forming a source-sink setting. To better understand magnetic properties in such settings, we studied red soil on lowmagnetic bedrock, and sub-recent sediments of Caohai Lake (CL) in Heqing Basin (HB), China. Red soil is the only important source material for the CL sediments, it is highly magnetic with susceptibilities (χ) of ~$10^{-5}m^3/kg$. The red soil is dominated by pedogenic nano-magnetite

(~10-15 nm) arranged in aggregates of ~100 nm, with particle interaction that causes a wide effective grain size distribution in the superparamagnetic (SP) range tailing into stable single domain (SSD) behavior. Transmission electron microscopy and broadband-frequency χ(f) suggest partial disintegration of the aggregates and increased alteration of the nanoparticles to hematite during transfer of red soil material to CL. This shifts the domain state behavior to smaller effective magnetic grain sizes, resulting in lower χfd% and χ values, and a characteristic change of χ(f). The SP-SSD distribution of the aggregates in red soil could be climate dependent, and the ratio of saturation remanence to χ is a potential bedrock-specific paleoclimate proxy reflecting it. Magnetic properties of the CL sediments are controlled by an assemblage of nanoparticle aggregates and larger sized bedrock-derived magnetite. The results challenge the validity of the previous paleoclimate interpretation from the 168-m long Core-HQ (900-30 ka) in HB. Disintegration of aggregates could lead to SP behavior with low χfd% without extinction of individual magnetite nanoparticles, and the χfd%-based assumption of SP magnetite dissolution may be wrong.

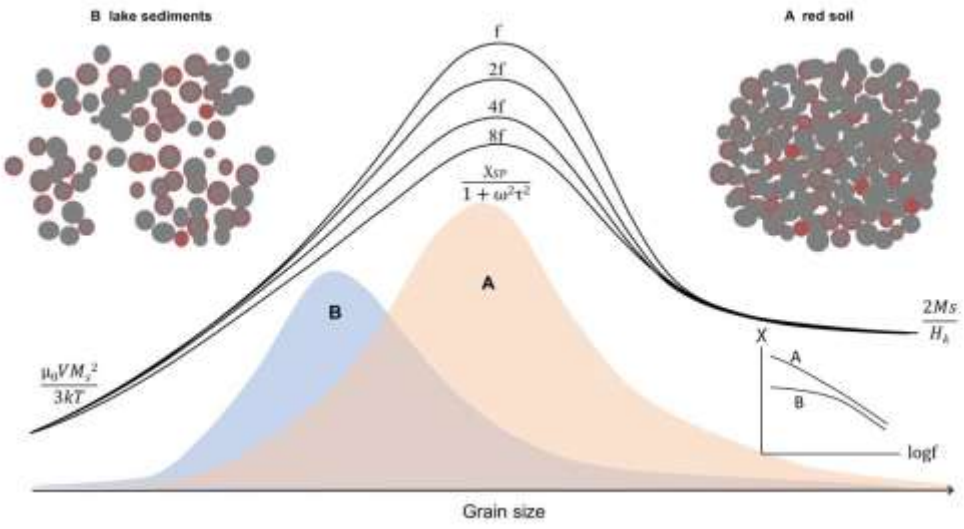

Figure 1. Conceptual sketch of the principle relationship of χ versus grain diameter (d) for four frequencies in logarithmically equal increments (increasing from f to 8f), modified from Kodama (2013), and following the theory presented by Worm (1998) and Shcherbakov and Fabian (2005). The principle relationships for smaller SP grains (below thermal activation), SP grains in the range of thermal activation (frequency-dependent; in-phase part), and larger grains in the SSD range are shown (Ms: saturation magnetization, H_k: microcoercivity, χ_{SP}: superparamagnetic susceptibility for zero

frequency, V: grain volume, τ: relaxation time, T: temperature, f: frequency, ω: angular frequency, μ0: magnetic permeability of free space, k: Boltzmann constant). The orange and gray fields display schematic distributions of effective grain sizes of the nano-magnetite aggregates in red soil (A) and lake sediments (B), respectively. Aggregates in red soil are assumed to be tighter packed and possibly also larger than in lake sediments, and according to the ELNES results more hematite is existing in the nanoparticles of the lake sediments.

13. 渤海表层沉积物磁性特征的物源意义

翻译人：李海 12031330@mail.sustech.edu.cn

Li M , Zhu S , Ouyang T , et al. Magnetic fingerprints of surface sediment in the Bohai Sea, China[J]. Marine Geology, 2020:106226.

https://doi.org/10.1016/j.margeo.2020.106226

摘要：为更好的了解周缘河流对渤海沉积物供给的影响。在次本研究中，对渤海与周缘河流表面沉积物进行磁学性质研究，用以解释渤海不同物源沉积物的分布。由磁学性质的不同将沉积物磁性矿物分出 7 个物源区。沉积物磁性矿物含量由边缘向中间减少的趋势。渤海中部与北部的沉积物中细颗粒磁性矿物含量高于南部。渤海西部（渤海西部和辽东湾）磁性矿物含量较高，因为其物源区含有大量具有磁铁矿的古老变质岩。沉积物供给量最高的黄河与渤海南部（主要在莱州湾西北部）的河流对细粒高矫顽力磁性矿物（例如赤铁矿）有贡献。由磁学性质的相似性可知，一些流域较小的河流（例如福州河）也是沿海水域磁性矿物的重要贡献者。黄海北部的沉积物在磁学性质与黄河碎屑沉积物相似。研究结果显示快速磁测可应用于物源示踪。

Abstract The understanding of the surrounding river impacts on the sediment supply to the Bohai Sea, northern China, is insufficient. In this study, magnetic measurements on surface sediment from the Bohai Sea and surrounding rivers were performed to interpret the distribution and origin of sediment in the Bohai Sea. Different magnetic properties in the analyzed material correspond to seven provenance areas. The magnetic mineral content decreases gradually toward the central Bohai Sea from its marginal areas. Sediment in the central and northern parts contains higher concentrations of finer magnetic minerals than the southern Bohai Sea. The western Bohai Sea (western Bohai and Liaodong bays) has high contents of magnetic minerals because its provenance areas contain abundant old metamorphic rocks with magnetite. The Yellow River, with the most elevated sediment flux, contributes with fine, high-coercivity magnetic minerals (e.g., hematite) to the southern Bohai Sea (mainly in the northwestern Laizhou Bay). Some local rivers (e.g., Fuzhou River) are also important contributors to the coastal waters, due to the magnetic similarities. Sediment from the north Yellow Sea is magnetically similar to the Yellow River detritus. The results highlight the use of the rapid magnetic method in provenance tracing.

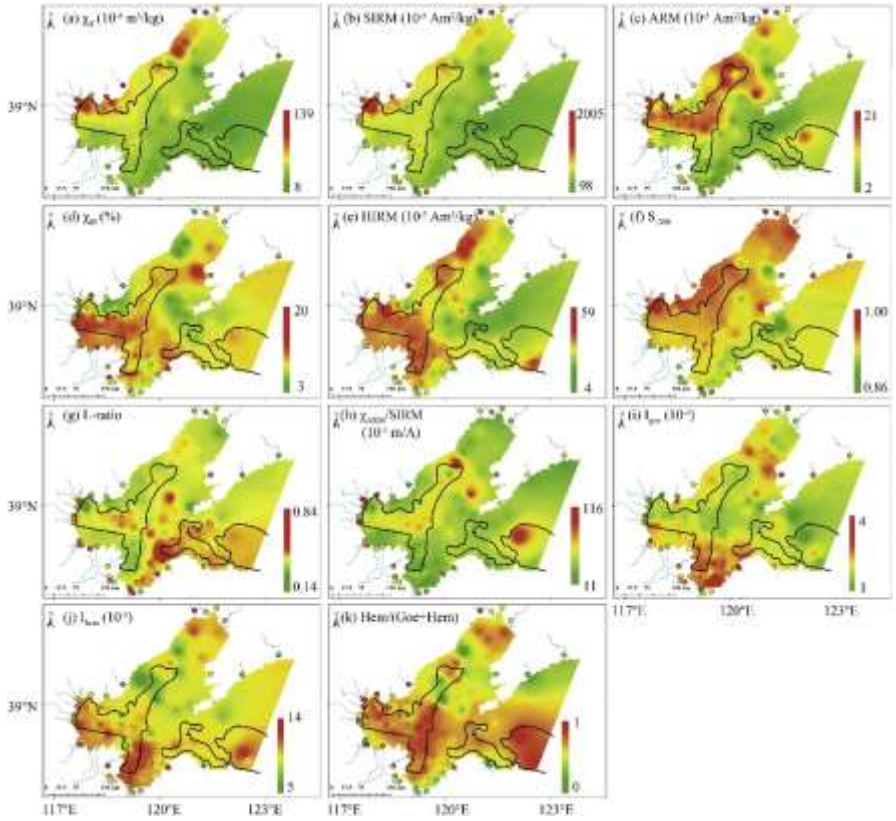

Figure 1. Spatial distributions of magnetic properties, including (a) χlf, (b) SIRM, (c) ARM, (d) χfd, (e) HIRM, (f) S−300, (g) L-ratio, (h) χARM/SIRM, (i) Igoe, (j) Ihem, and (k) Hem/(Goe + Hem). Solid dots show values for the surrounding rivers. The two mud areas (defined by Mz more than 6φ) were delineated by black lines.

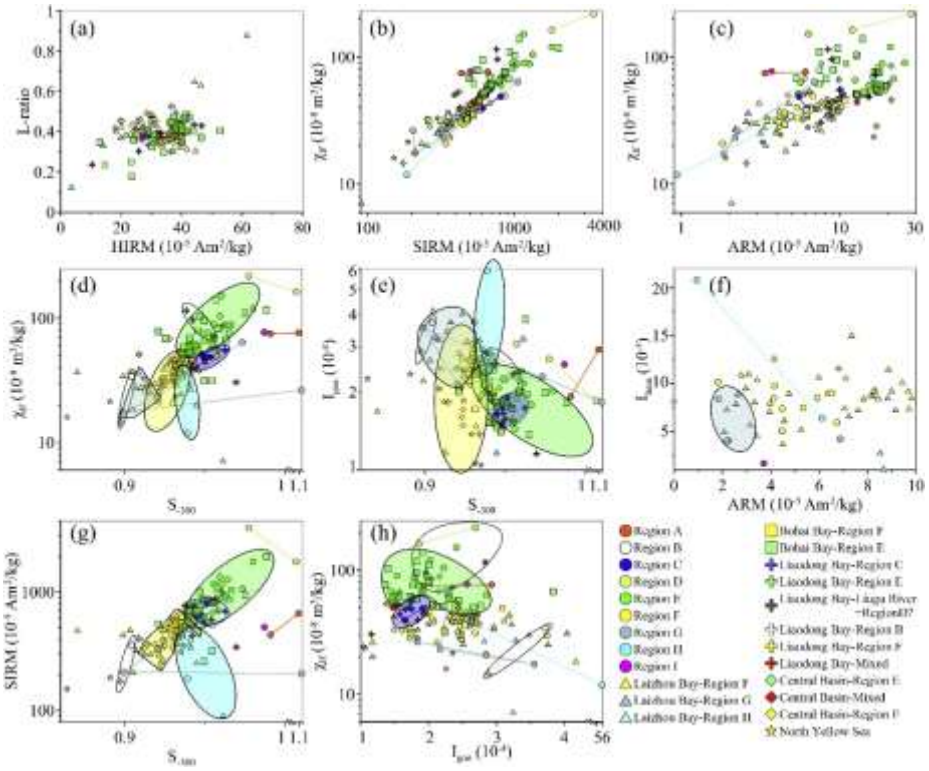

Fig. 2 Scatter plots of (a) HIRM and L-ratio, (b) χ_{lf} and SIRM, (c) χ_{lf} and ARM, (d) χ_{lf} and S−300, (e) I_{goe} and S−300, (f) I_{hem} and ARM, (g) SIRM and S−300, and (h) χ_{lf} and I_{goe}. Possible provenances are delineated.

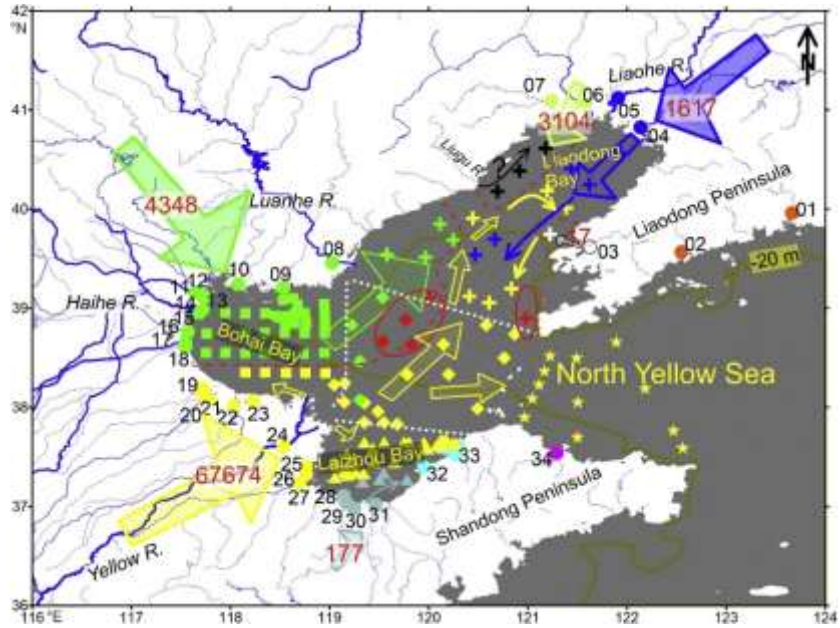

Fig. 3 Transport pathways in the Bohai Sea. Dashed red and dotted white lines represent provenance and geographical boundaries, respectively. Arrows with varied colors stand for sediment input and transport directions, and numbers on the arrows denote the annual fluvial sediment load in 104 t/a. Red solid lines delineate the regions of mixed sources.

14. 南大洋对流作用加大了南极变暖和 HS4 时期大气 CO_2 的增加

翻译人：张亚南 zhangyn3@mail.sustech.edu.cn

Luke Skinner, Laurie Menviel, Lauren Broadfield et al., ***Southern Ocean convection amplified past Antarctic warming and atmospheric CO_2 rise during Heinrich Stadial 4*** *[J]. Communications Earth & Environment, 2020, 23.*

https://doi.org/10.1038/s43247-020-00024-3

摘要：古气候记录中所凸显的周期性和强烈的千年尺度异常，以两极“跷跷板”模式的温度变化为特征，被认为是由大西洋径向翻转流的快速变化引起。通过抑制北大西洋对流强度，可以模拟出热量两极跷跷板模式变化的特征；然而却未能通过两极冰芯钻孔得到这种幅度的温度变化。这里，我们通过对深海温度的重建，结合氧化还原条件和放射性 C 通风年龄记录去验证特别强烈的千年尺度异常和 H4 时期南大洋深层对流增强的存在。我们的结果强调了南大洋对流的增强对南极变暖和大气 CO2 增加潜在的放大作用，是对源自北大西洋的触发作出的反应。

ABSTRACT: The record of past climate highlights recurrent and intense millennial anomalies, characterised by a distinct pattern of inter-polar temperature change, termed the ‘thermal bipolar seesaw’, which is widely believed to arise from rapid changes in the Atlantic overturning circulation. By forcing a suppression of North Atlantic convection, models have been able to reproduce many of the general features of the thermal bipolar seesaw; however, they typically fail to capture the full magnitude of temperature change reconstructed using polar ice cores from both hemispheres. Here we use deep-water temperature reconstructions, combined with parallel oxygenation and radiocarbon ventilation records, to demonstrate the occurrence of enhanced deep convection in the Southern Ocean across the particularly intense millennial climate anomaly, Heinrich Stadial 4. Our results underline the important role of Southern Ocean convection as a potential amplifier of Antarctic warming, and atmospheric CO2 rise, that is responsive to triggers originating in the North Atlantic.

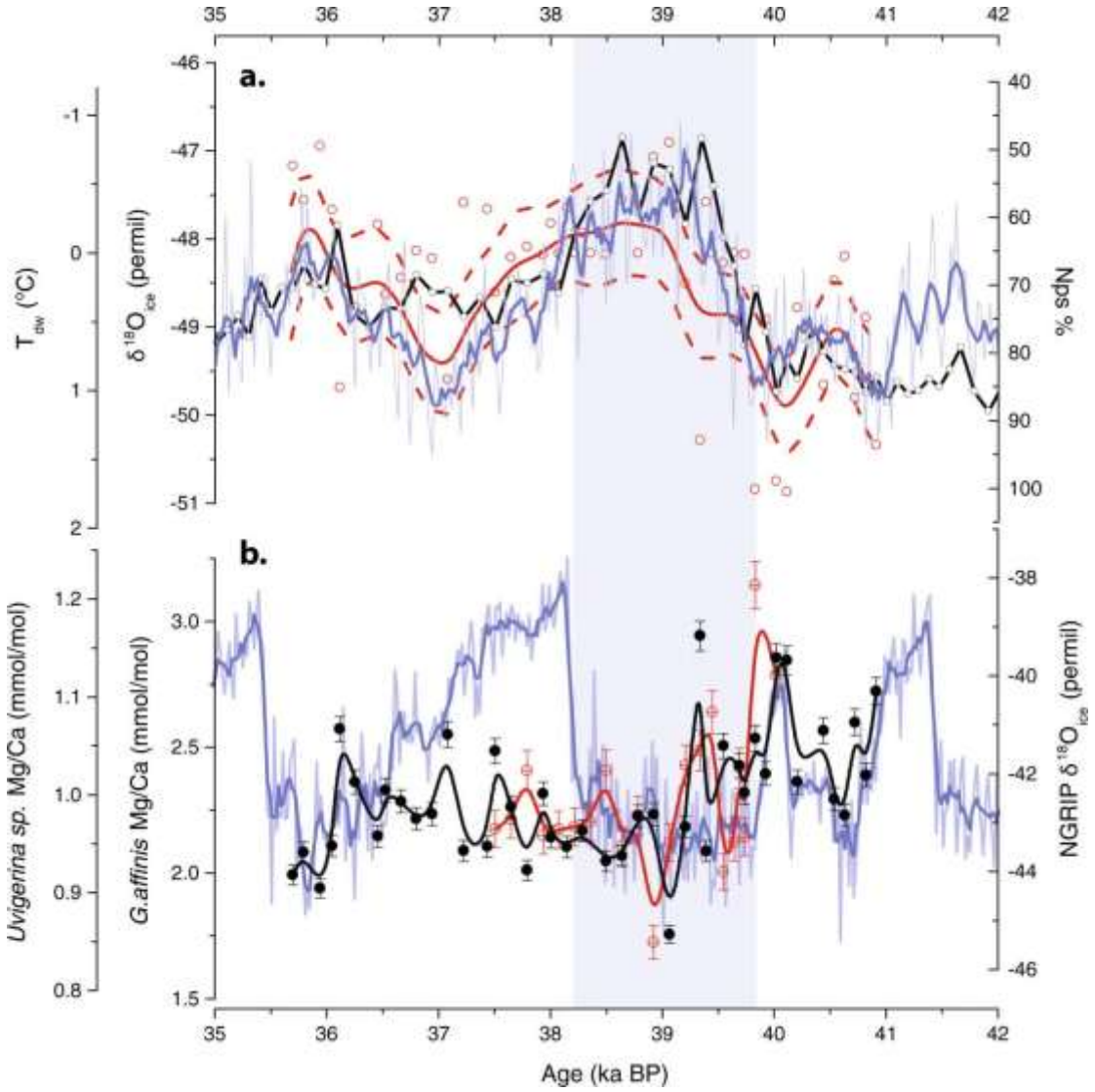

Figure 1. Down-core *G. affinis* and *Uvigerina sp.* Mg/Ca results, compared with the Greenland and Antarctic ice-core event stratigraphies. **a** Polar planktonic foraminifer, *N. pachyderma* (left coiling) abundance (black solid line and open circles, Nps %), compared with the EDML Antarctic ice-core temperature proxy, $\delta^{18}O_{ice}$ (blue line), and with deep-water temperature variability estimated from combined Mg/Ca measurements from two benthic foraminifer species (open red circles, with cubic spline and 95% confidence intervals, based on 0.6 °C 1 sigma uncertainty, are indicated by the solid and dashed red lines respectively; note inverted y axis). **b** benthic Mg/Ca measurements (*G. affinis*, solid black circles and spline; *Uvigerina sp.*, crossed red circles and spline; error bars represent 2% analytical reproducibility), compared with the Greenland ice-core temperature proxy $\delta^{18}O_{ice}$ (light blue line, with dark blue running mean). Vertical shaded bar indicates the approximate timing of Heinrich Stadial 4 (HS4).

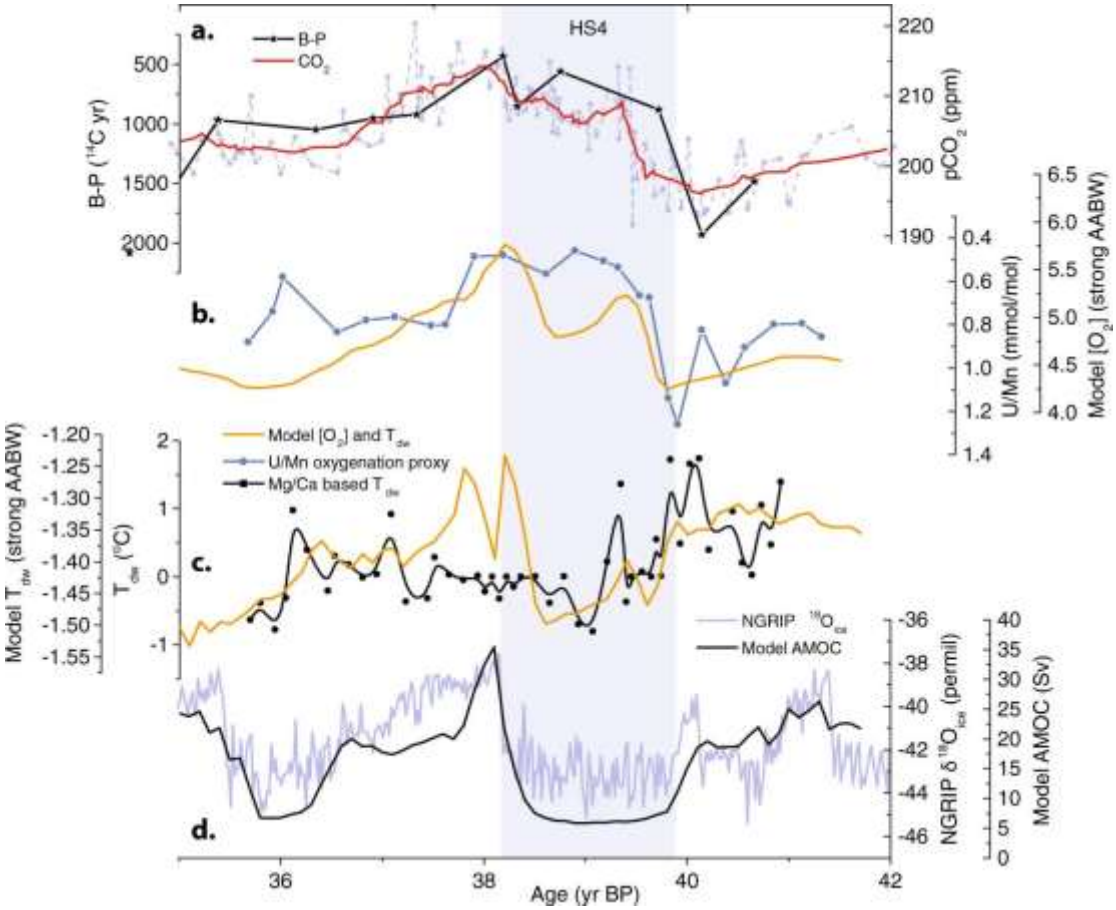

Figure 2. Comparison of reconstructed and modelled deep-water temperatures and ventilation. Data from MD07-3076Q are compared with composites of simulations performed with the UVic and LOVECLIM Earth system models (experiments U-TrS and L-TrS from ref. 12), and atmospheric CO2 change. **a** Atmospheric CO2 (light blue filled circles and dashed line, and solid red line showing 3-point smoothing), compared with deep-water radiocarbon ventilation inferred from B-P radiocarbon age offsets37. **b** Reconstructed oxygenation based on authigenic U/Mn ratios of foraminiferal coatings37 (solid blue circles and line), compared with simulated Southern Ocean deep-water oxygenation (solid orange line), based on a composite of outputs over 55–10 ° W, 50–75 ° S and 3300–4000 m. **c** Reconstructed deep-water temperature based on benthic Mg/Ca (filled black circles, and b-spline solid line), compared with simulated Southern Ocean deep-water temperature (solid orange line). **d** Greenland δ18Oice event stratigraphy compared with simulated maximum Atlantic Meridional Overturning Circulation (AMOC) stream-function (solid black line).

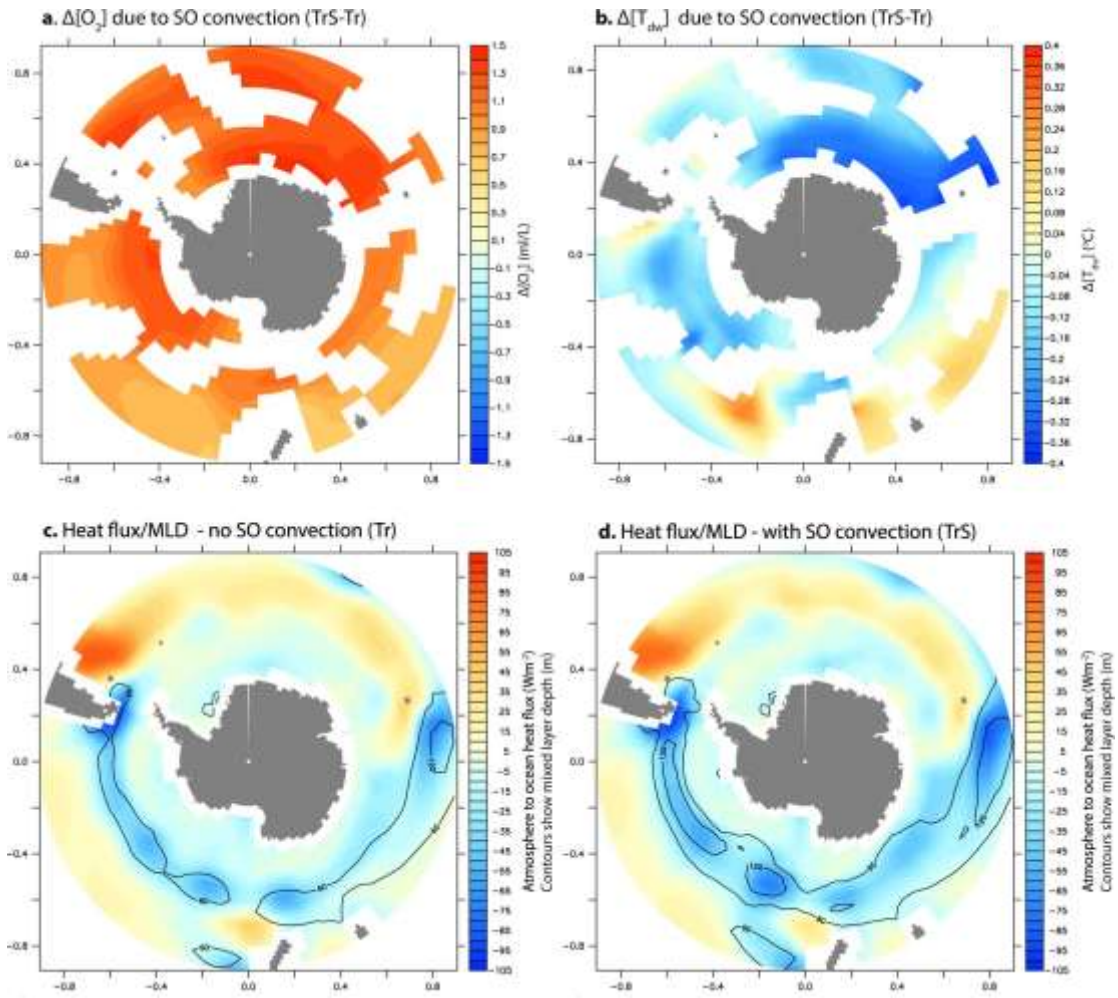

Figure 3. The thermal- and oxygenation 'fingerprint' of enhanced Southern Ocean convection, based on numerical model simulations. **a** Impact of enhanced convection on deep-water oxygenation (3300–4000 m depth), based on the difference between composites of UVic and LOVECLIM simulations of HS4 with- (Tr–S) and without (Tr) enhanced Southern Ocean convection; **b** as for (**a**) but for deep-water temperature; **c** atmosphere to ocean heat flux (shading; negative values indicate increased heat flux out of the ocean), and mixed layer depth (MLD, contours) for composite of UVic and LOVECLIM simulations of HS4, without enhanced Southern Ocean convection; **d** as for (**c**), but for simulations with enhanced Southern Ocean convection.

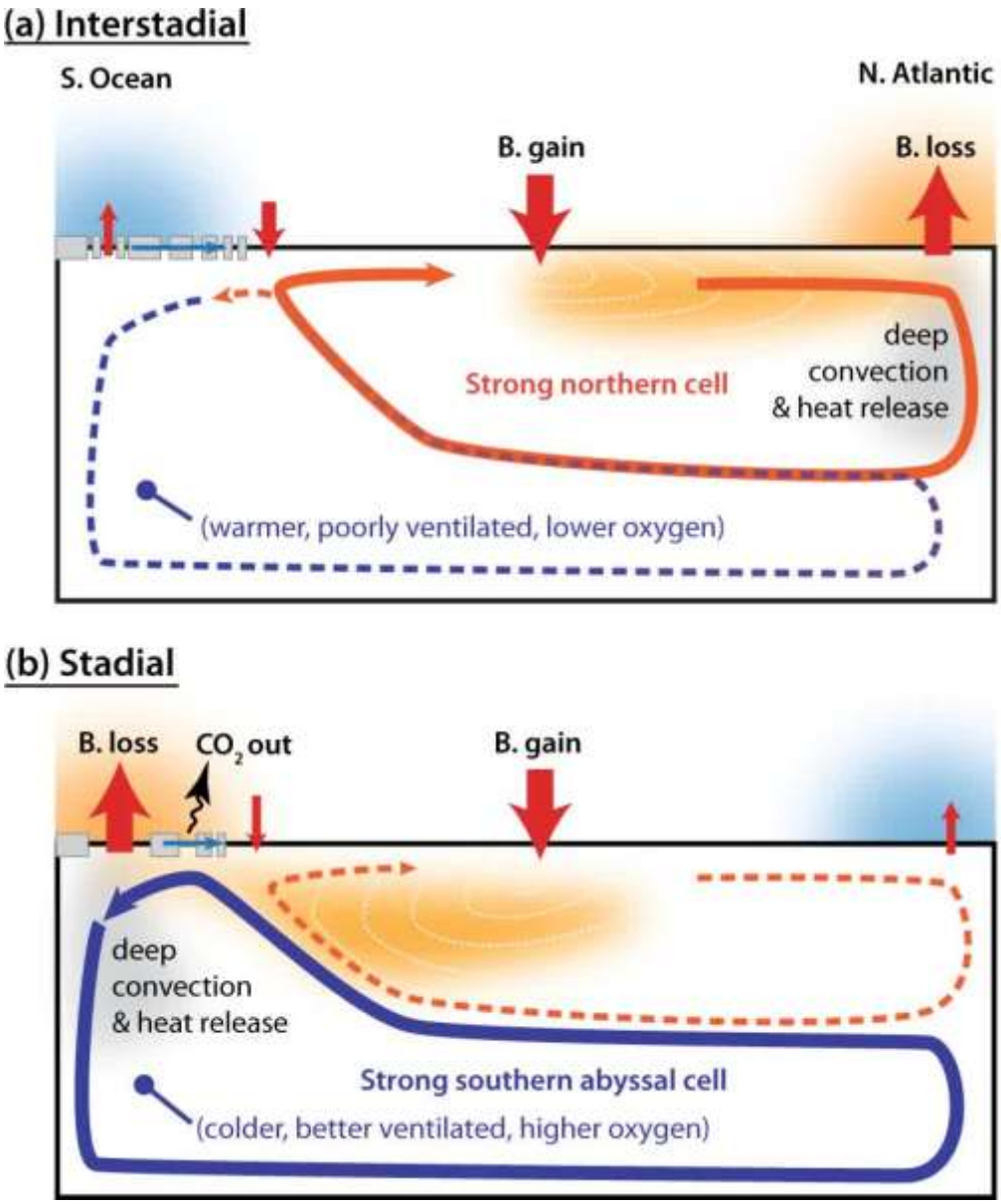

Figure 4. Schematic of the bipolar 'ventilation seesaw' concept. An alternating dominance of buoyancy (and heat) loss from the North Atlantic (right) and Southern Ocean (left), balances buoyancy and heat input at low latitudes, for **a** Greenland-interstadial, and **b** Greenland-stadial conditions. Enhanced air–sea exchange associated with water-mass conversion in the Southern Ocean enhances heat- and carbon loss from the southern abyssal cell, and increases its oxygen and radiocarbon content (note that the northern cell will typically remain warmer and better ventilated than the abyssal southern cell). Red arrows at the ocean surface indicate buoyancy fluxes of different approximate magnitudes. Weakened overturning cells are indicated by dashed continuous arrows; strengthened cells by heavy solid continuous arrows.